Chapter 5

Exploration of Fluorescence Behavior of Imidazolium-based Chemosensor and its "Turn-on" Response for Al^{3+} in Pure Aqueous Medium

5.1 Introduction

Aluminium is the third most abundant element comprising 8% of the earth's crust and is the widely used metal [1]. Aluminium and its alloys have diverse uses in packaging, consumer durables, transportation industry, construction, energy generation, electrical transmission, and machinery [2]. An elevated amount of aluminium as ionic Al^{3+} becomes a highly toxic and ubiquitous pollutant [3-5]. Al^{3+} can interact with biological species and adversely affect their functioning. The aluminium precipitation on the gills of fish causes ionoregulatory, osmoregulatory dysfunction, and several respiratory problems. This acute toxicity originates due to the binding of aluminium to the gill epithelium and intracellularly within lamellar epithelial cells [6]. Al^{3+} adversely affects the uptake and transport of essential nutrients in land plants, thus affecting the cell division in root tip and lateral roots and increases the rigidity of DNA double helix by reducing DNA replication [7]. Al^{3+} is widely known as a neurotoxin leading to neurodegeneration and affects more than 200 important biological reactions. Most of these reactions influence the mechanisms related to brain development, such as axonal transport, synaptic transmission, neurotransmitter synthesis, protein degradation, phosphorylation or de-phosphorylation of proteins, gene expression and peroxidation. Al^{3+} is also responsible for brain diseases including Alzheimer′s, Parkinson′s and multiple sclerosis [8-9].

The potential toxic effects of Al^{3+} on human beings and the environment have stimulated present ongoing research to develop potent methods for the detection of Al^{3+}. Traditional analytical techniques for detecting Al^{3+} ions include electrochemistry, chromatography, graphite furnace atomic absorption spectrometry, inductively coupled plasma mass spectroscopy, voltammetry, and spectrophotometry. However, these methods suffer from disadvantages such as complex procedures, time-consuming sample preparation, and expensive equipment which limit their applications [10-12]. The fluorescence-based chemosensing for detection of Al^{3+} is also a popular method due to its simplicity, non-destructive nature, superior sensitivity, high selectivity, instant response, and real-time detection. In 1867, F. Goppelsröder reported the first example of fluorescent chemosensor for Al^{3+} ion which formed a highly fluorescent morin chelate [13-14]. Generally, fluorescent chemosensors induce a change in fluorescence wavelengths or emission intensities after their interaction with analyte *via* different photophysical mechanisms, including photoinduced

electron transfer (PET), C=N isomerization, and chelation induced enhanced fluorescence (CHEF).

PET involves an excited electron transfer from the free receptor to fluorophore molecule under the UV-visible light. On the absorption of a photon, the electron in fluorophore is excited and transferred from HOMO to the LUMO level (**Figure 5.1**). The left vacant space is then filled by an electron from the HOMO of free receptor molecule that results in fluorescence quenching. Binding to electron-deficient species (e.g. cation, anion, etc.) raises the redox potential of bound receptor and lower the energy of the HOMO level as a result PET is inhibited and the fluorescence intensity is enhanced [15].

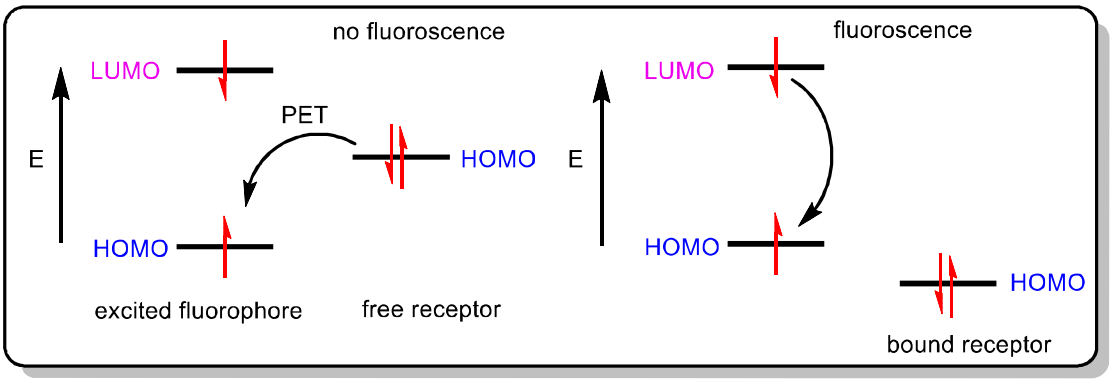

Figure 5.1 Schematic representation of PET process

Schiff bases exhibit the C=N isomerization process which effectively consumes the energy of excited states and makes them non-emissive in solution resulting in weak fluorescence emission. However, when the non-bonding electrons of imine nitrogen atom coordinate with a metal ion, structural rigidity is induced which blocks the non-radiative pathways, thereby enhancing the fluorescence intensity. This phenomenon is known as the CHEF process (**Figure 5.2)** [16-17].

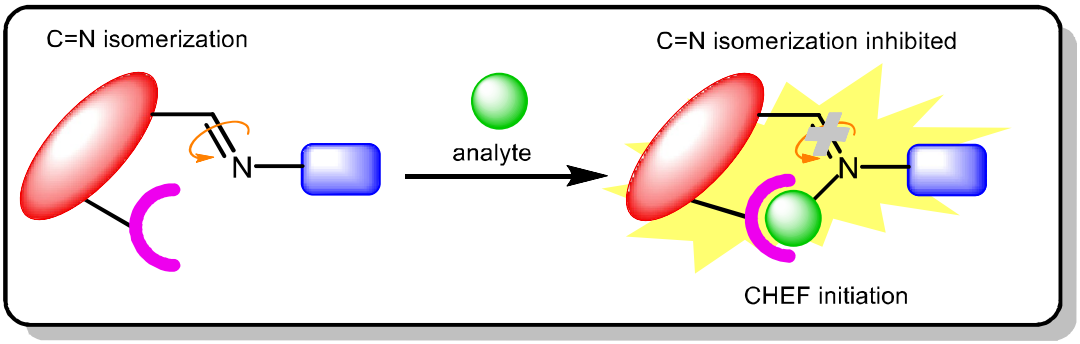

Figure 5.2 Schematic representation of C=N isomerization and CHEF processes

These aforementioned mechanisms have provided opportunities to design fluorogenic chemosensors for fast and effective detection of metal ions. Considerable efforts have been made towards designing fluorescence turn-on chemosensors based on hydrazone, rhodamine, azobenzene, coumarin, naphthalimide, etc. for the selective detection of Al^{3+} ions. Lee and coworkers reported a tripeptide (SerGluGlu) based chemosensor **1** (**Figure 5.3**) attached with a dansyl fluorophore for selective detection of Al^{3+}. The binding studies suggested that the carboxyl and hydroxyl groups of the peptide receptor are involved in the coordination with Al^{3+} resulting in turn-on fluorescence response [18]. Yeap *et al.* synthesized a chalcone based chemosensor {1-[3-(2-Hydroxy-phenyl)-3-oxopropenyl]-naphthalen-2-yloxy}-acetic acid **2** (**Figure 5.3**) based on CHEF. They proposed that the chalcone group acts as a fluorophore unit and carboxyl group increased hydrophilicity and being a hard base provided binding sites for selective detection of hard acid Al^{3+} [19].

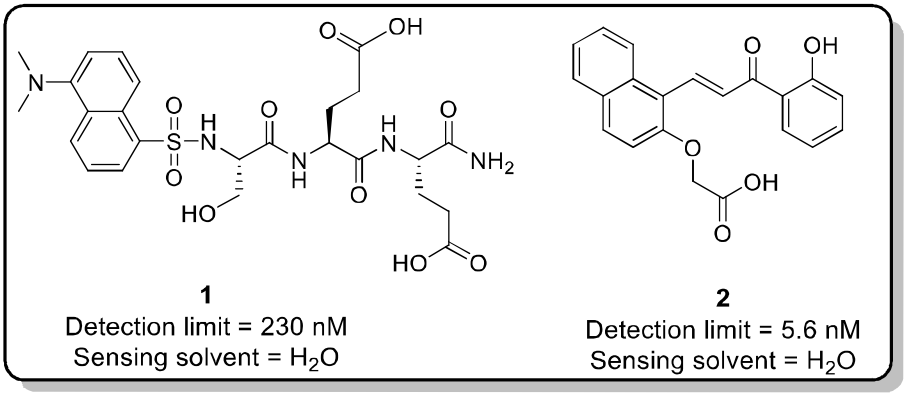

Figure 5.3 Tripeptide- (**1**) and Chalcone- (**2**) based chemosensors

Jain and coworkers reported a colorimetric and turn-on fluorescent chemosensor **3** (**Figure 5.4**) based on 1-(2-pyridylazo)-2-naphthol for the selective detection of Al^{3+}. Under the UV lamp, the colourless methanolic solution of chemosensor showed pinkish-red fluorescence on the addition of Al^{3+} within 5s [20]. Khurana and coworkers synthesized PET-based turn-on fluorescent as well as colorimetric chemosensor **4** (**Figure 5.4**) based on ampyrone moiety linked to sesamol *via* azo linker for the selective sensing of Al^{3+} [21]. Goswami and coworkers reported 5-methyl-1-pyridin-2-yl-1H-pyrazole-3-carboxylic acid (1-pyridin-2-yl-ethylidene)-hydrazide probe **5** (**Figure 5.4**) for selective fluorescent turn-on response for Al^{3+} detection involving CHEF mechanism. The bioimaging studies on HepG2 cells demonstrated real-time detection of Al^{3+} in living cells [22].

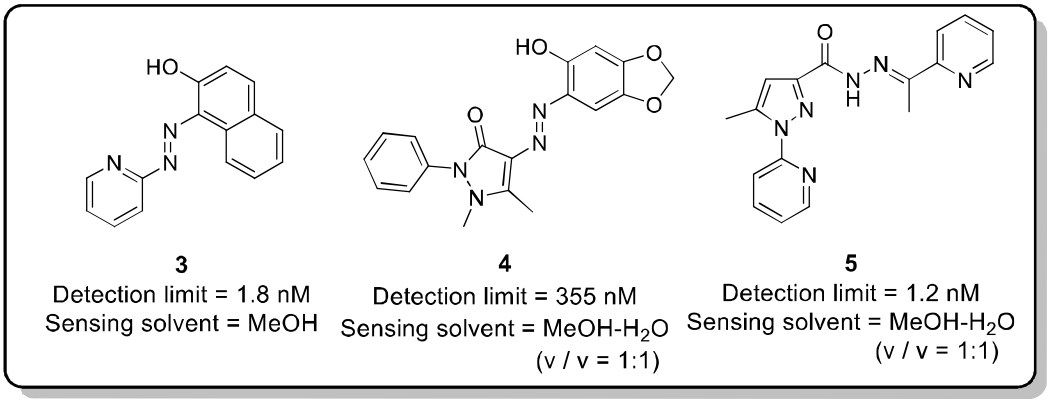

Figure 5.4 Azo- (**3** and **4**) and Hydrazide- (**5**) based chemosensors

Wang *et al.* reported tetrabenzoyl hydrazone-TPE chemosensor **6** (**Figure 5.5**) exhibiting fluorescence turn-on response for Al^{3+} by inhibiting PET and C=N isomerization processes [23]. Velmathi and coworkers synthesized two phenazine based imidazole fluorescent chemosensors **7a** and **7b** (**Figure 5.5**) for selective detection of Al^{3+}. On the addition of Al^{3+}, aggregation-induced emission by restriction of intramolecular rotation resulted in fluorescence enhancement [24].

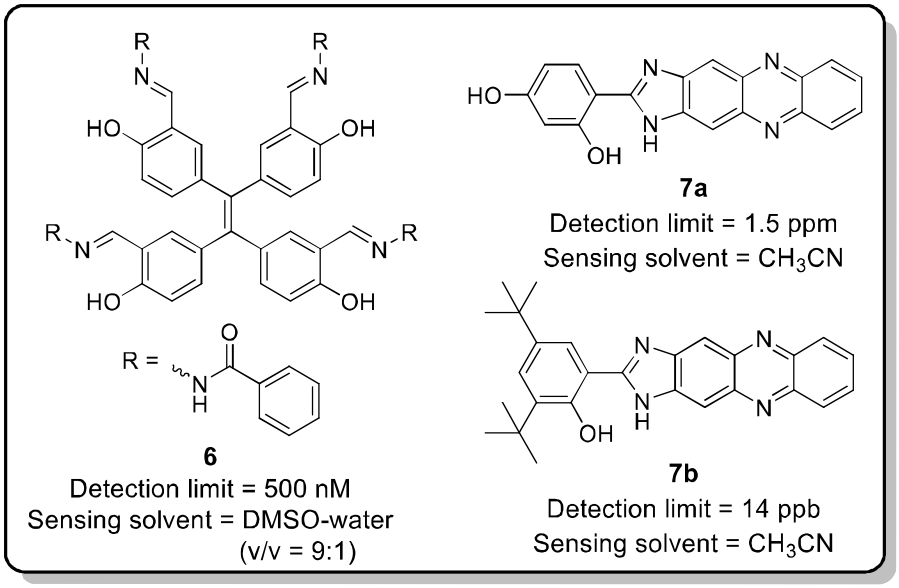

Figure 5.5 Hydrazone- (**6**) and Phenazine- (**7**) based chemosensors

Liu *et al.* reported a water-soluble host-guest system based on *β*-cyclodextrin and organic molecule derived from 4-(diethylamino)-2-hydroxy-benzaldehyde and carbohydrazide (**8a**), and another same type of host-guest system with organic molecule derived from paeonol and anthraniloyl hydrazine (**8b**) (**Figure 5.6**) for selective detection of Al^{3+} [25-26].

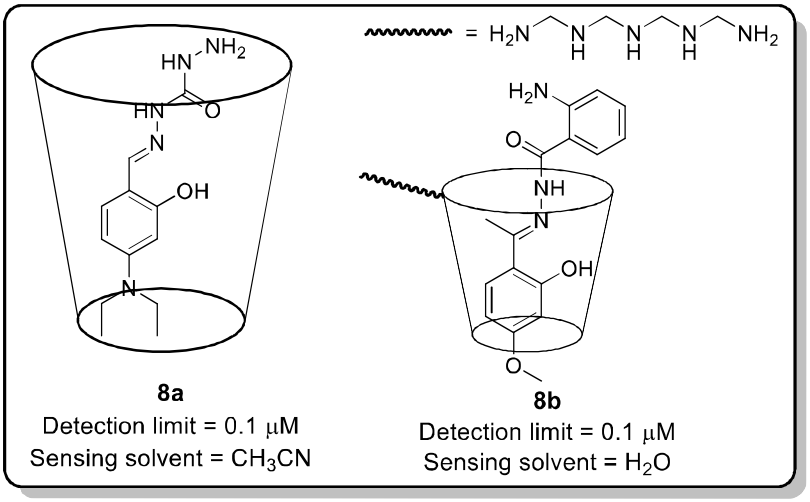

Figure 5.6 *β*-cyclodextrin-based chemosensors (**8a** and **8b**)

The photophysical behaviour of Schiff bases has been studied extensively due to their unique optical properties which are widely applicable in the field of optical data storage, molecular electronics, and sensors [27]. Schiff bases derived from 2-hydroxybenzaldehyde is an interesting research area due to the presence of O···H-N and O-H···N type hydrogen bonds as well as keto-enamine and enol-imine tautomerization. Considerable attempts have been made to study the keto-enol stability of 2-hydroxybenzaldehyde derived Schiff bases in solution and solid-state. Most of these exist in both form (keto and enol) in the solution, while in solid-state keto form is more stable [28-29]. They offer structural and cavity control of host-guest complexation resulting in good selectivity, sensitivity, and stability for a particular ion and therefore have been extensively employed as chemosensors. By incorporating more N or O donor atoms, Schiff bases form strong complexes with metal ions and are employed as ionophore in optical sensing of different cations [30-32]. Chellappa and coworkers reported the synthesis of 5-((anthracen-9-ylmethylene)amino)quinolin-10-ol fluorescent probe **9** (**Figure 5.7**) for selective detection of Pb^{2+} and Al^{3+}. The live-cell imaging studies suggested the effective monitoring of Pb^{2+}/Al^{3+} in MCF-7 cells [33]. Yan *et al.* proposed a coumarin and L-histidine based Schiff base fluorescent chemosensor **10** (**Figure 5.7**) for selective sensing of Al^{3+} by inhibiting the PET process. L-histidine enhanced the water solubility, the nitrogen atoms in L-histidine and the hydroxyl group in the coumarin acted as receptor units for Al^{3+} binding [34]. Saha and coworkers synthesized 5-(2-phenyldiazenyl)-2-hydroxy-3-methoxybenzaldehyde chemosensor **11** (**Figure 5.7**) exhibiting 61-fold fluorescence enhancement on binding with Al^{3+} by CHEF process [35]. Wu *et al.* synthesized an Al^{3+} selective fluorescent probe **12** (**Figure 5.7**) containing 1,8-naphthalimide moiety as a

fluorophore and Schiff base as a recognition group. The probe also effectively monitored Al^{3+} in river and tap water samples [36].

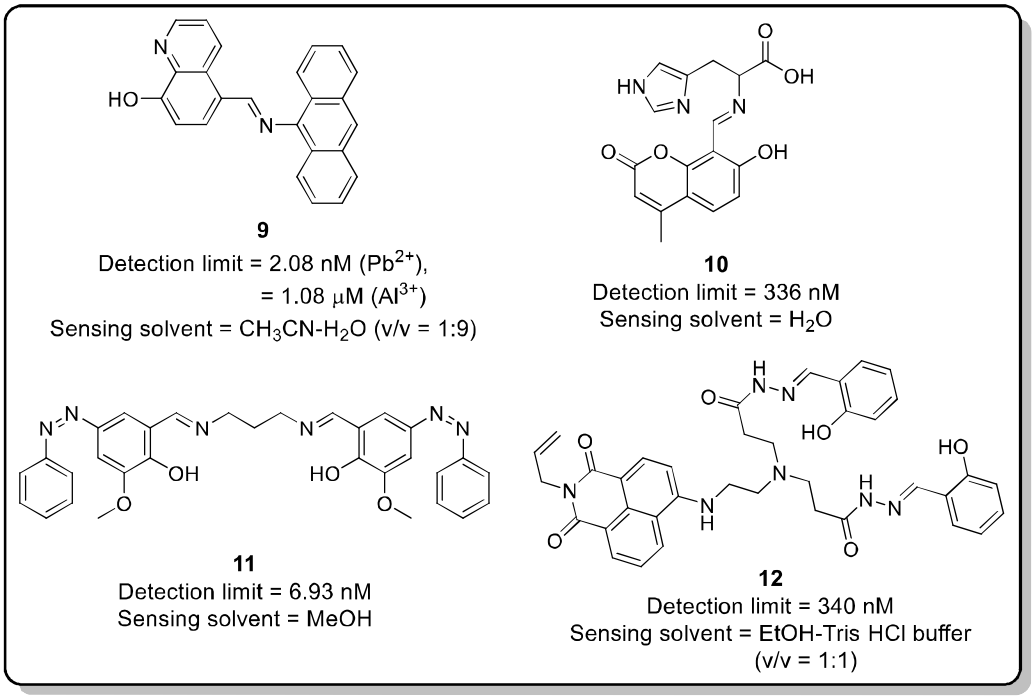

Figure 5.7 Anthracene- (**9**), Coumarin- (**10**), *o*-vanillin- (**11**) and Naphthalimide- (**12**) based Schiff base chemosensors

Dey and coworkers proposed (1-[(4,6-dimethyl-pyrimidin-2-yl)-hydrazonomethyl]-naphthalen-2-ol) fluorescent chemosensor **13** (**Figure 5.8**) for selective detection of Al^{3+} *via* turn-on mechanism due to the restriction in PET and ESIPT (Excited state intramolecular proton transfer) processes. For real applications the monitoring of intracellular Al^{3+} in human embryonic kidney cell lines, HEK293 was performed [37]. Upadhyay and coworkers synthesized two chemosensors **14a** and **14b** based on naphthalene sulfonic acid skeleton (**Figure 5.8**) for the fluorogenic detection of Al^{3+}. The fluorescence enhancement after Al^{3+} addition was attributed to the restriction of C=N isomerization and inhibition of PET and ESIPT process due to CHEF. The detection of Al^{3+} was also conducted on test paper strips [38]. Goswami and coworkers developed benzophenone based Schiff base chemosensor 2-[(2-Hydroxy-ethylimino)-phenyl-methyl]-phenol **15** (**Figure 5.8**) for selective detection of Al^{3+} by the inhibition of C=N isomerization and ESIPT resulting in activation of CHEF. The chemosensor was also used to detect Al^{3+} in the HepG2 cell line [39]. Leng *et al.* developed two novel rhodamine-based fluorescent chemosensors **16a** and **16b** (**Figure 5.8**) and proposed that upon Al^{3+} addition the enhancement in fluorescence was observed due to the unfolding of

spirolactam ring with restriction in C=N isomerization. For biological applications, the MTT assays and cell imaging experiments for Al^{3+} monitoring was conducted in SGC-7901 living cells [40].

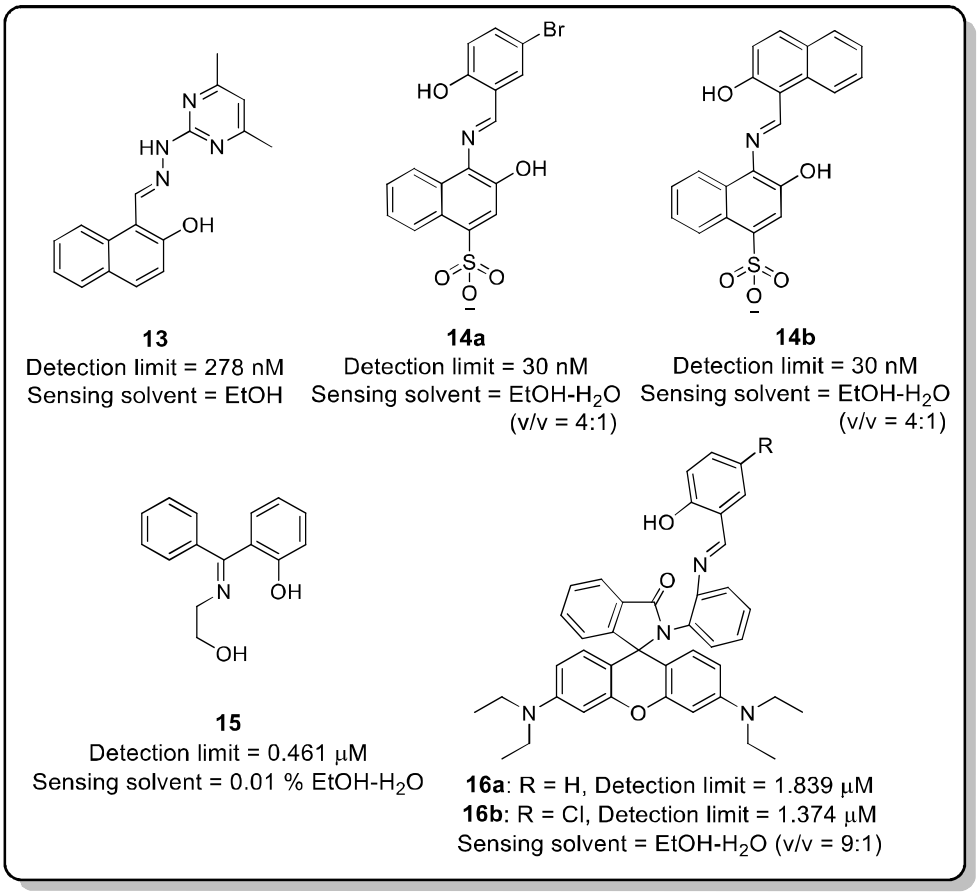

Figure 5.8 Hydrazinopyrimidine- (**13**), Naphthalene sulfonic acid- (**14a-b**), Benzophenone- (**15**), Rhodamine B- (**16**) based Schiff base chemosensors

Being an important class of heterocyclic chemistry, aminoquinolines exhibit the excellent chelating ability and act as chromogenic and fluorogenic chemosensors for the selective detection of Zn^{2+}, Cd^{2+}, Hg^{2+}, nitric oxide ($NO^{\bullet}$), HSO_3^- (bisulfite), $C_2O_4^{2-}$ (oxalate), $P_2O_7^{4-}$ (pyrophosphate) and glucosamine [41-47]. Schiff bases having aminoquinoline as amine source possess excellent fluorescence response due to their unique chemical interaction with various metal ions (Zn^{2+}, Cu^{2+}, Pb^{2+}, Cd^{2+}, Hg^{2+}, and Mg^{2+}) [48-52]. Aminoquinoline based Schiff base chemosensors are also widely explored for Al^{3+} detection. Roy *et.al* prepared 1-((quinolin-3-ylimino)methyl)naphthalen-2-ol chemosensor **17** (**Figure 5.9**) primarily for the sensing of Al^{3+} and the resulting aluminium complex worked as a secondary sensor for F^- ion. Under the UV irradiation, the methanolic solution of chemosensor containing Al^{3+} showed

bluish-green colour which further changed to violet colour on the addition of F^- [53]. They also documented the synthesis of two positional isomers, 4-methyl-2-((quinolin-6-ylimino)methyl)phenol **18a** and 4-methyl-2-((quinolin-2-ylimino)methyl)phenol **18b** (**Figure 5.9**) for the selective sensing of Al^{3+} and Zn^{2+} [54]. The cell imaging studies for the intracellular Zn^{2+} and Al^{3+} detection was also conducted on C6 cells. Huang *et.al* synthesized 2-aminoquinoline and napthaldehyde derived Schiff base chemosensor **19** (**Figure 5.9**) for selective detection of Al^{3+} [55]. The fluorescent probe was also used to detect Al^{3+} in real samples like blood, urine, and tap water. Kindy *et al*. reported napthaldehyde and 8-aminoquinoline based Schiff base chemosensor **20** (**Figure 5.9**) for selective sensing of Al^{3+} in acetate buffer solution at pH 5.5. This method was also applied for the determination of Al^{3+} in drinking water and pharmaceutical samples [56].

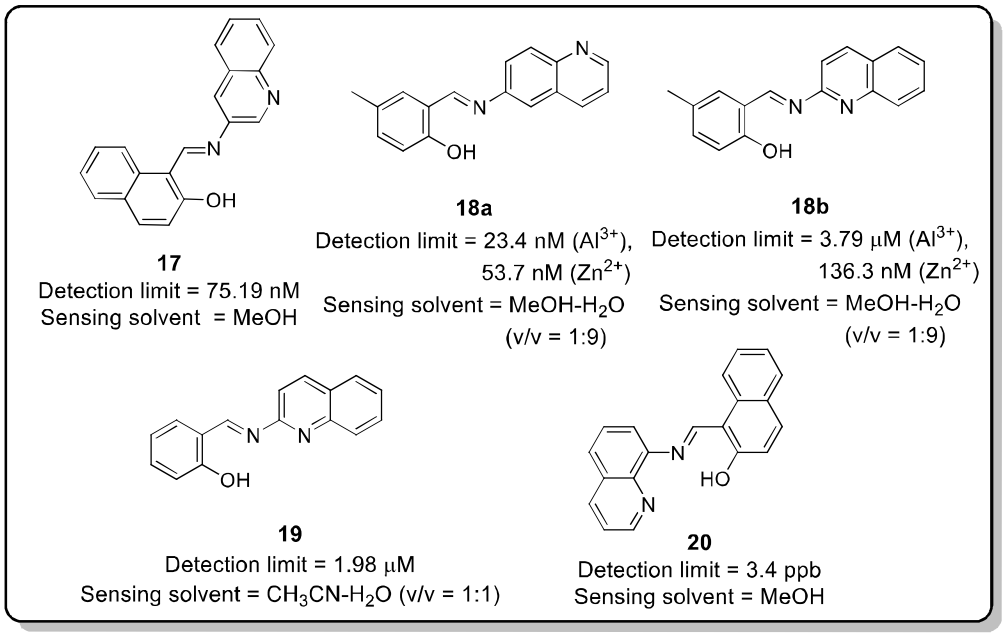

Figure 5.9 Aminoquinoline-based Schiff base chemosensors (**17-20**)

The lower solubility of chemosensors in aqueous media hampers their applications for biological and environmental samples. This limitation can be circumvented by using hydrophilic imidazolium-based chemosensors [57-58]. These chemosensors can be easily synthesized by their facile introduction to organic moiety *via* simple nucleophilic substitution of the halogen group [59]. In literature, some imidazolium-based chemosensors are reported for the detection of different metal ions in the aqueous medium. Singh and coworkers proposed chemosensor **21** based on benzothiazole moiety connected to imidazolium *via* an ether linkage (**Figure 5.10**), that primarily detected Hg^{2+} in water and the resultant Hg^{2+} complex worked as

a ratiometric sensor for Br^- ions. ^1H NMR studies suggested that the imidazolium hydrogen in the Hg^{2+} complex participated in the recognition of Br^- ions. The detection of Hg^{2+} and Br^- was also conducted in river and tap water samples [60]. Zhou *et al.* proposed a series of cyclophane fluorescent chemosensors **22a-c** (**Figure 5.10**) containing acridine moiety connected to imidazolium through ether linkage which exhibited good selectivity for Fe^{3+} and $H_2PO_4^-$ ions in water and acetonitrile solutions, respectively. Fe^{3+} was detected *via* turn-off fluorescence, whereas $H_2PO_4^-$ exhibited a yellow-green fluorescence due to turn-on response [61].

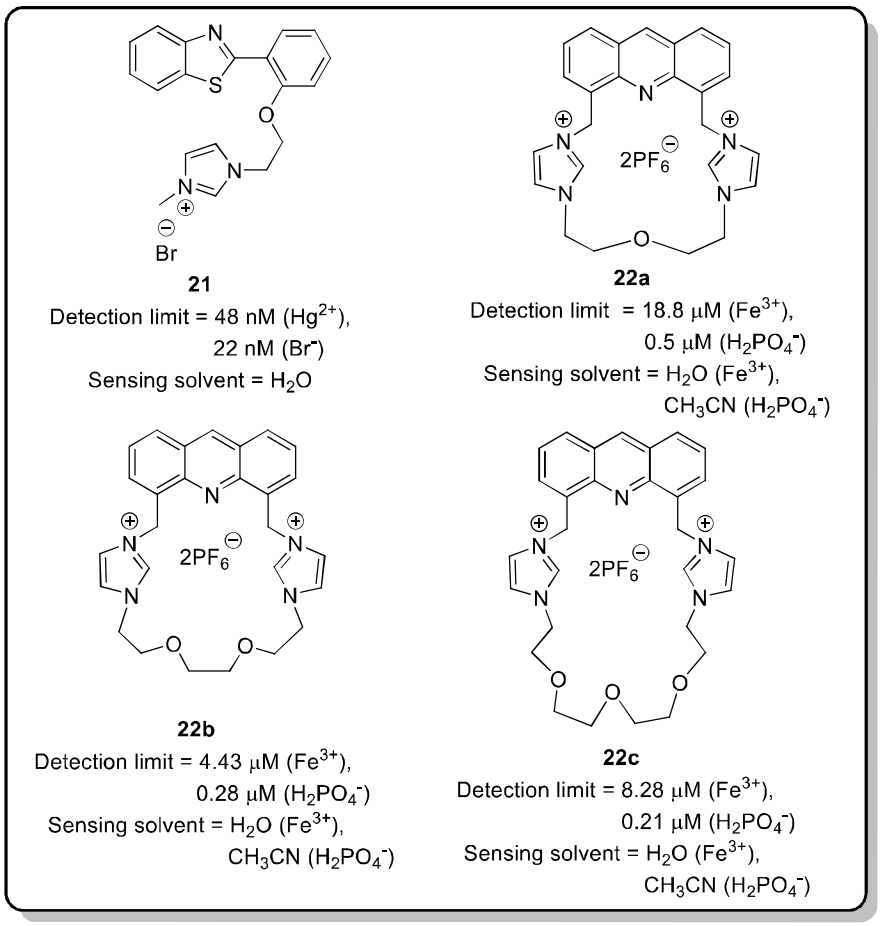

Figure 5.10 Benzothiazole- (**21**) and Cyclophane-based (**22a-c**) chemosensors

The majority of chemosensors have limitations of involving multiple synthetic steps, poor selectivity, low sensitivity, and weak fluorescence response. Furthermore, their water insolubility requires the use of organic co-solvent, which hampers their on-site real-time applications. Thus, an imidazolium-based Schiff base chemosensor (**ImSB**) having hydrophilic property and ONN skeleton for effective metal binding is developed.

5.2 Results and discussion

5.2.1 Synthesis and characterization of ImSB

The synthetic route for the preparation of imidazolium-based **ImSB** utilizes the Schiff-base condensation approach as given in **Scheme 5.1**.

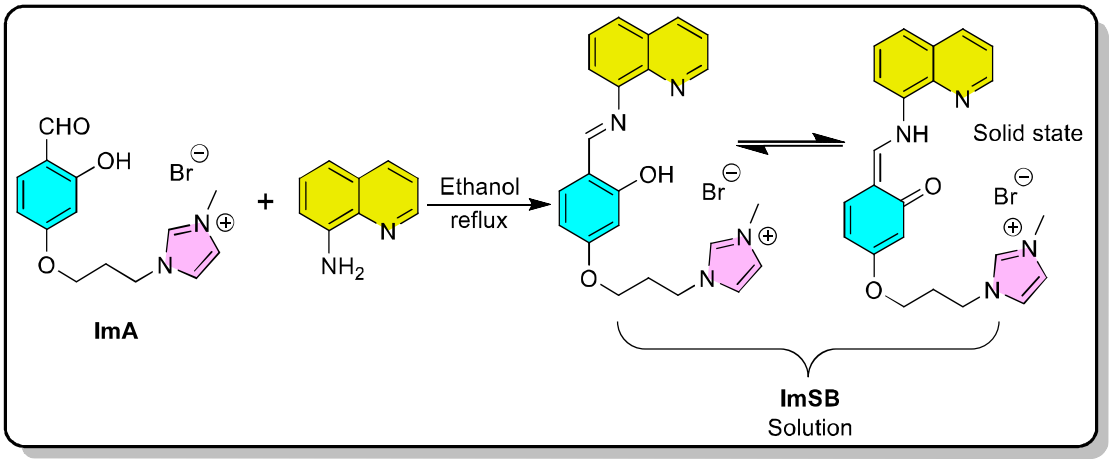

Scheme 5.1 Synthesis of chemosensor **ImSB**

The FTIR and X-ray crystallographic characterization suggested the existence of keto tautomer of **ImSB** in solid-state. In the IR spectrum, broadening of $\nu_{(N-H)}$ stretching vibrations due to the intramolecular hydrogen bonding was observed in region 3300-3400 cm^{-1}. A sharp peak at 1610 cm^{-1} for the carbonyl $\nu_{(C=O)}$ stretching and another peak at 1571 cm^{-1} due to imine $\nu_{(C=N)}$ stretching of quinoline moiety were observed (**Figure 5.11**).

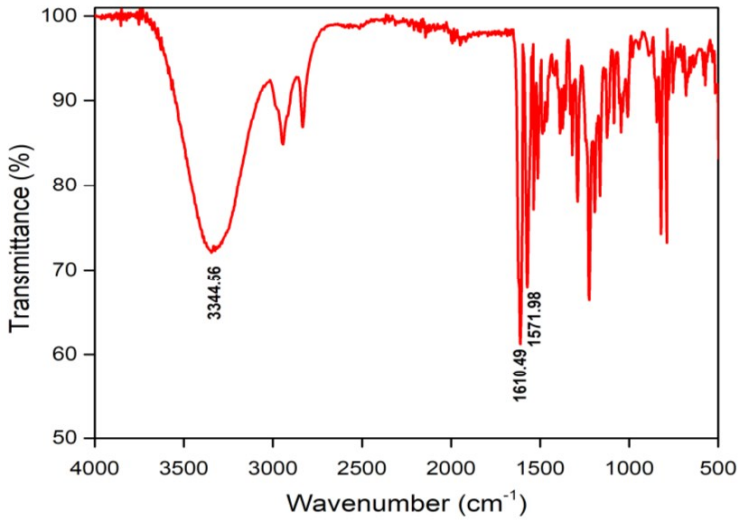

Figure 5.11 IR spectrum of **ImSB**

The X-ray diffraction studies suggested that **ImSB** crystallizes in the triclinic crystal system and *P*-1 space group. The single-crystal XRD data and cell parameters are summarized in **Table 5.1** and the ORTEP diagram is given in **Figure 5.12**.

Table 5.1 Crystal data and structure refinement of **ImSB**

Identification code	**ImSB**
Empirical formula	$C_{23}H_{25}BrN_4O_3$
Formula weight	485.38
Temperature/K	293
Crystal system	Triclinic
Space group	*P*-1
a/Å	9.2780(3)
b/Å	10.9501(2)
c/Å	11.6256(3)
α/°	87.339(2)
β/°	68.312(2)
γ/°	88.577(2)
Volume/Å^3	1096.27(5)
Z	2
ρcalcg/cm^3	1.470
μ/mm^{-1}	1.908
F(000)	500.0
Crystal size/mm^3	0.2 × 0.2 × 0.1
Radiation	MoKα (λ = 0.71073)
2Θ range for data collection/°	6.222 to 59.698
Index ranges	-12 ≤ h ≤ 12, -13 ≤ k ≤ 14, -16 ≤ l ≤ 14
Reflections collected	16387
Independent reflections	5523 [R_{int} = 0.0214, R_{sigma} = 0.0219]
Data/restraints/parameters	5523/0/289
Goodness-of-fit on F^2	1.058
Final *R* indexes [I>=2σ (I)]	R_1 = 0.0224, wR_2 = 0.0566
Final *R* indexes [all data]	R_1 = 0.0264, wR_2 = 0.0582
Largest diff. peak/hole / e Å^{-3}	0.38/-0.21

[a] $R_1 = \sum||F_o| - |F_c||/\sum|F_o|$. [b] $wR_2 = [\sum w(F_o^2 - F_c^2)^2/\sum w(F_o^2)^2]^{1/2}$, where $w = 1/[\sigma^2(F_o^2) + (aP)^2 + bP]$, $P = (F_o^2 + 2F_c^2)/3$.

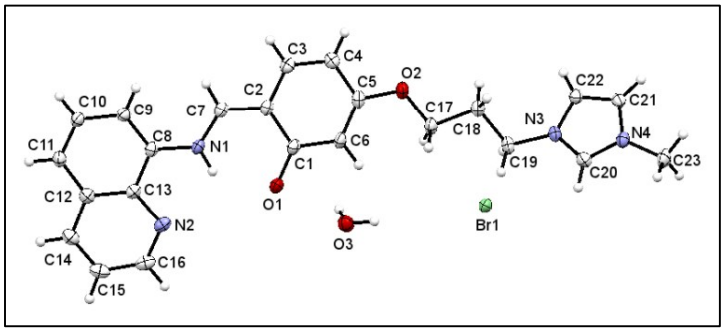

Figure 5.12 ORTEP diagram of **ImSB** drawn with a 50% ellipsoidal probability

The Schiff base enamine N(1)=C(7) bond and N(1)–C(8) bond lengths are 1.3241(17) and 1.4075(16) Å, respectively. The quinolone ring N(2)–C(13) and N(2)-C(16) bond lengths are 1.3663(16) and 1.3186(18) Å, respectively. The ketonic O(1)–C(1) bond, ether O(2)–C(5), and O(2)-C(17) bond lengths are 1.2779(16), 1.3595(15) and 1.4255(16) Å, respectively. The C(21)=C(22) of the imidazolium ring is the shortest carbon to carbon distance (1.3566(18) Å) in this molecule. Intramolecular hydrogen bonding N(1)—H(1)---O(1) of 2.00 Å and 133.2°, and intermolecular hydrogen bonding C(22)—H(22)---O(1) of 2.27 Å and 165.6° can be observed **(Table 5.2)**. The quinolone ring plane and phenyl ring plane are 14.91° to each other. The dihedral angles C(13)–C(8)–N(1)–C(7) and C(8)–N(1)–C(7)–C(2) and C(3)–C(2)–C(7)–N(1) are 165.28°, -173.54° and 177.94°, respectively. Two molecular cations, two bromide ions, and two water molecules are occupied in a unit cell packing **Figure 5.13**.

Table 5.2 Hydrogen Bonds of **ImSB**

D	H	A	d(D-H)/Å	d(H-A)/Å	d(D-A)/Å	D-H-A/°	Symmetry
N(1)	H(1)	O(1)	0.86	2.00	2.6634(14)	133.2	-
C(22)	H(22)	O(1)	0.93	2.27	3.1837(16)	165.6	1+x,+y,+z

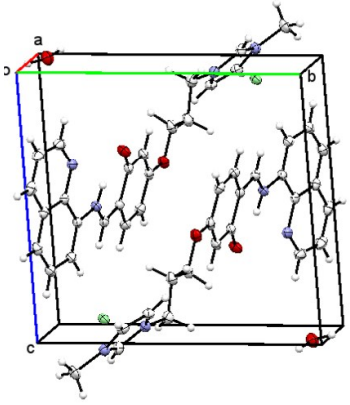

Figure 5.13 Unit cell packing of **ImSB**

One molecular salt with a water of hydration $[C_{23}H_{23}N_4O_2]^+Br^-.H_2O$ appears in the asymmetric unit (**Figure 5.14a**). The packing of molecules is around the c axis (**Figure 5.14b**) and the pair of organic molecular ions are arranged in head to tail fashion with weak $\pi\cdots\pi$ stacking interactions of middle phenyl rings of two molecules at a distance of 3.587 Å between the centroids (**Figure 5.14c**). The packing environment of molecules is ladder type with strong interactions between ketonic O(1)-atom of one molecule and H(22)-atom of imidazolium ring of the other molecule at 2.275 Å, which helps in the formation of J-aggregated structure [62] (**Figure 5.14d**).

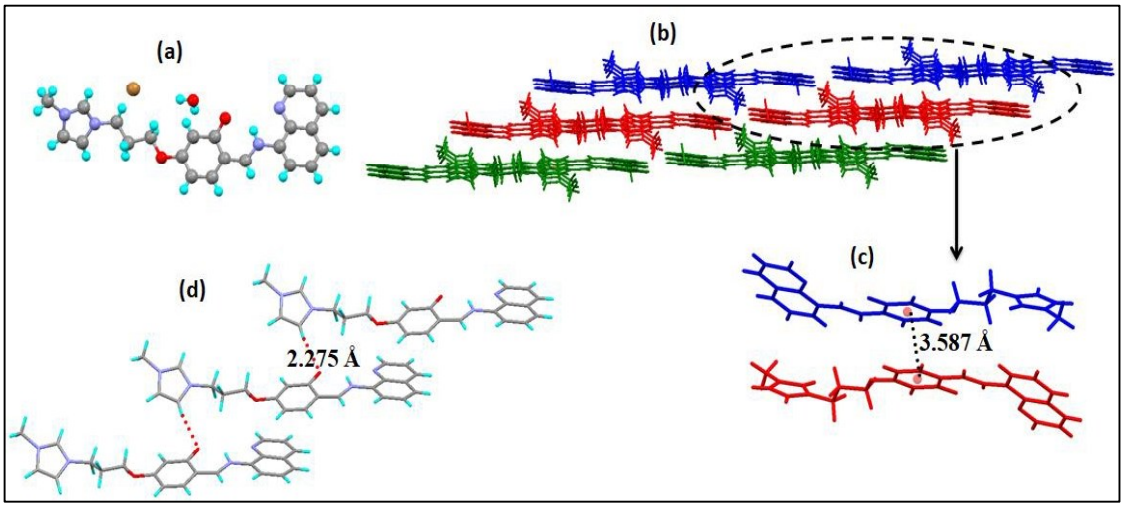

Figure 5.14 Crystal description of **ImSB** (**a**) asymmetric unit (**b**) packing arrangement of molecules (**c**) $\pi\cdots\pi$ interaction between the centroids of two molecules (**d**) staircase or ladder-type packing of molecules

The ^1H and ^{13}C NMR spectroscopy revealed that **ImSB** exists as enol form in the solution (DMSO-d_6). The ^1H NMR signal for azomethine proton of Schiff base appeared at 9.04 ppm and HC=N proton signal for quinoline moiety was detected at 8.98 ppm. The phenolic -OH proton singlet due to intramolecular hydrogen bonding with imine nitrogen appeared in the downfield region at 14.84 ppm (**Figure 5.15**). In ^{13}C NMR the signals at 160.9 ppm and 150.9 ppm also confirmed the presence of the C=N group of the Schiff base and quinoline moiety, respectively (**Figure 5.16)**. The HRMS of **ImSB** exhibited a peak at *m/z* = 387.1824 due to [**ImSB** - Br]$^+$ (**Figure 5.17**).

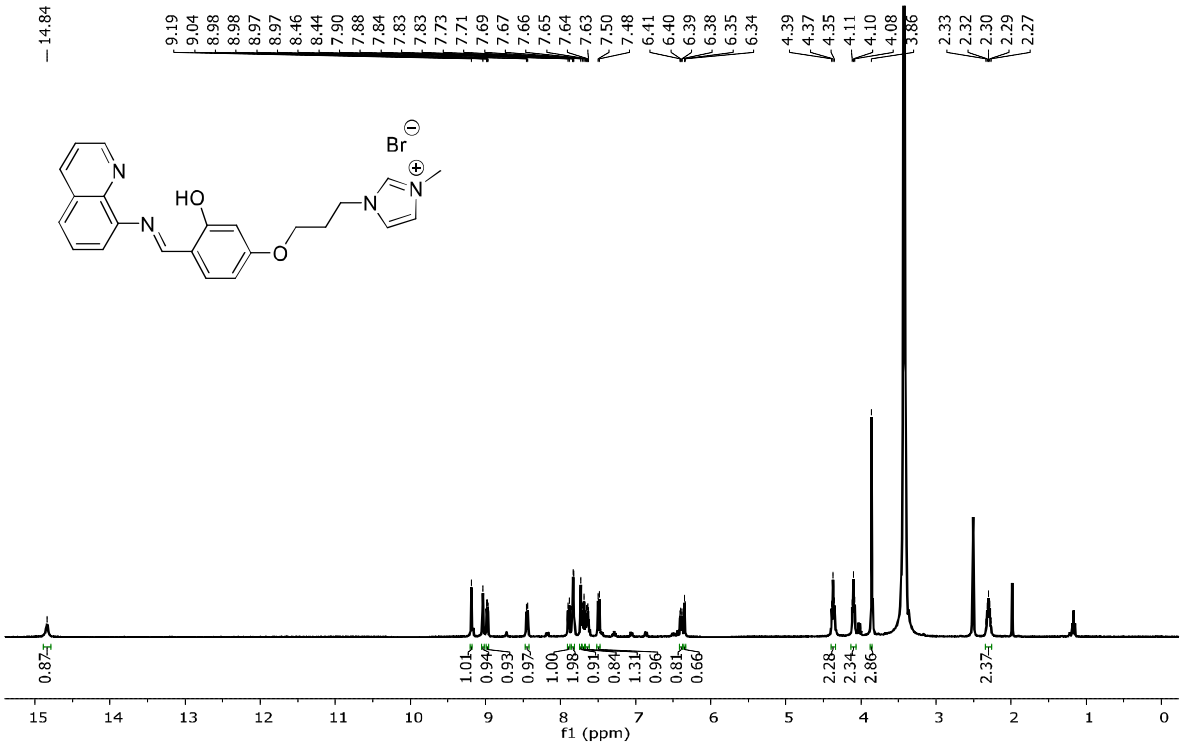

Figure 5.15 ^{1}H NMR spectrum of **ImSB** (DMSO-d_6)

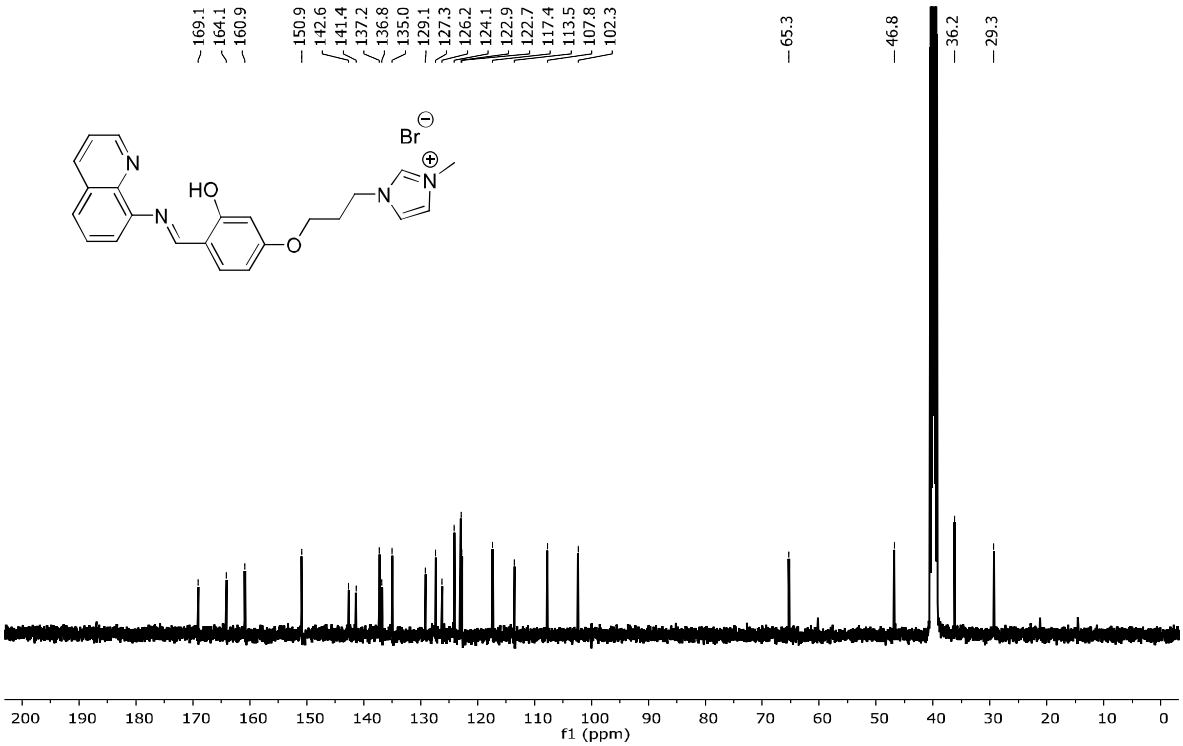

Figure 5.16 ^{13}C NMR spectrum of **ImSB** (DMSO-d_6)

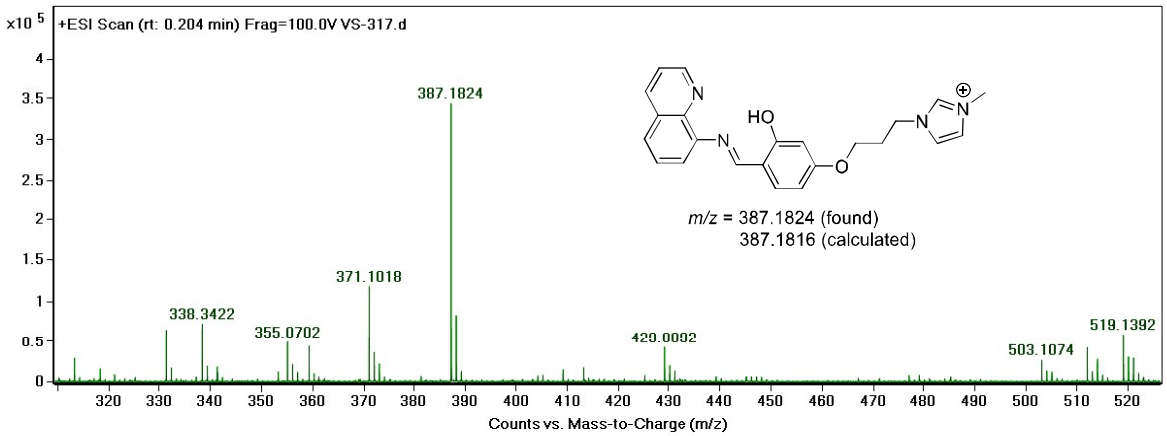

Figure 5.17 HRMS of **ImSB**

5.2.2 Photophysical properties of ImSB in solutions and solid-state

The UV-visible spectra of **ImSB** in water, MeOH, and DMSO were recorded at 10^{-4} M concentration (**Figure 5.18a**). In water and methanol, two absorption bands under 200-400 nm are assigned for π-π* and n-π* transitions of enol-imine form and one absorption band over λ_{max} = 400 nm to the keto-enamine form [63-64]. At 10^{-3} M **ImSB** concentration, an intense absorption band (λ_{max} = 425 nm) which diminished gradually on decreasing the concentration (10^{-5} M) suggested that enol form is more prominent at a lower concentration in water (**Figure 5.18b**). In polar aprotic solvent, no absorption band was observed above 400 nm region indicating the presence of only enolic form, ^{1}H and ^{13}C NMR spectra in the DMSO further supported the same finding.

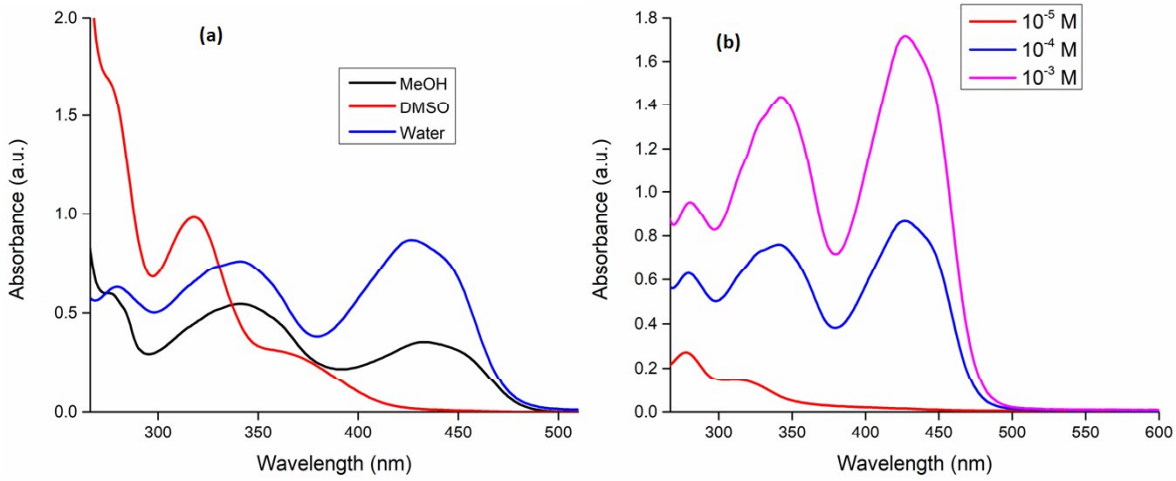

Figure 5.18 UV-visible spectra of **ImSB** (**a**) in different solvents at 10^{-4} M (**b**) at different concentrations in water

In the solid-state UV-visible spectra of **ImSB**, absorption bands were observed at 351 nm, 436 nm, and 509 nm (**Figure 5.19**).

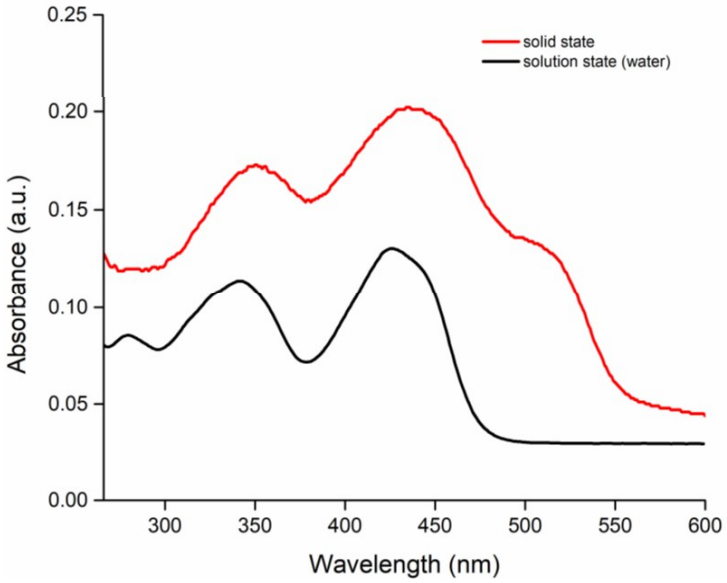

Figure 5.19 Solution (10^{-4} M) and solid-state UV-visible spectra of **ImSB**

The emission spectra at different concentrations of **ImSB** in the water at λ_{ex} = 410 nm were recorded. A sharp emission peak at λ_{em} = 477 nm due to the enol form appeared at 10^{-6} M, which on increasing concentration diminished. A new peak at λ_{em} = 502 nm due to keto form started appearing at 10^{-5} M and its maximum emission intensity was observed at 10^{-3} M (**Figure 5.20a-d**).

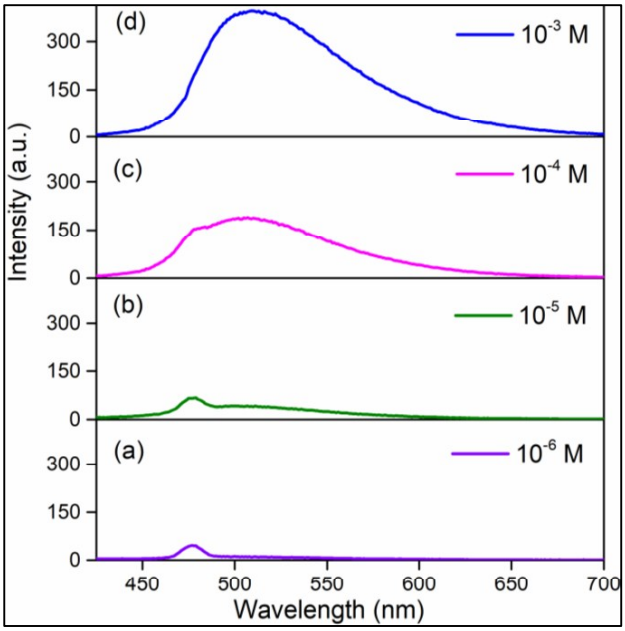

Figure 5.20 Fluorescence spectra at different concentrations of **ImSB** in water

At 10^{-2} M concentration and in solid-state, **ImSB** showed a red-shifted peak around λ_{em} = 554 nm (**Figure 5.21**). The appearance of the red-shifted absorption band (λ_{max} = 509 nm) and emission peak (λ_{em} = 554 nm) supported the formation of J-aggregation in solid [65].

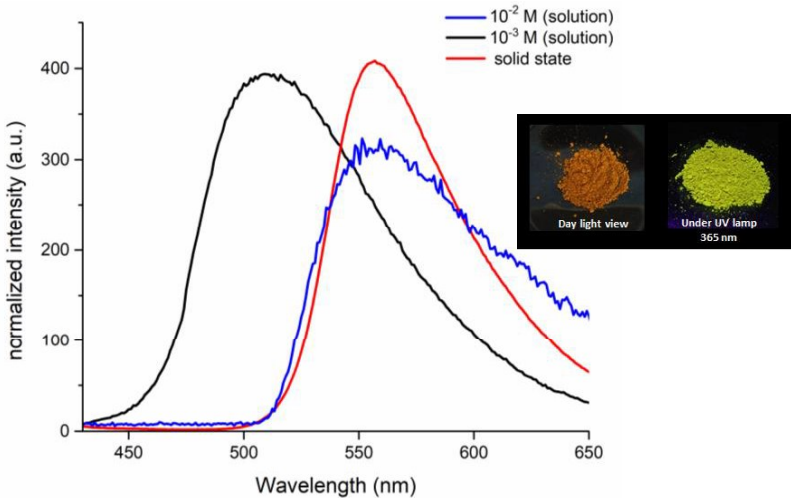

Figure 5.21 Solution (water) and solid-state fluorescence spectra of **ImSB**

The effect of pH on **ImSB** (50 μM) was also studied, at pH = 3-4 only one absorption band (λ_{max} = 312 nm), at pH = 7 two absorption bands (λ_{max} = 312 nm and 425 nm) and at pH = 9-10 one absorption band (λ_{max} = 359 nm) were observed. These observations suggested that at low pH enol form is present, at pH = 7 both keto and enol forms exist. At high pH due to the deprotonation of a hydroxyl group, the presence of keto form becomes more favourable and shifting of the peak to 359 nm may be due to *cis* or *trans* isomerization (**Figure 5.22a**). The fluorescence spectra also suggested the presence of enol form at pH = 3-4 and both keto and enol forms at pH = 7-10 (**Figure 5.22b**).

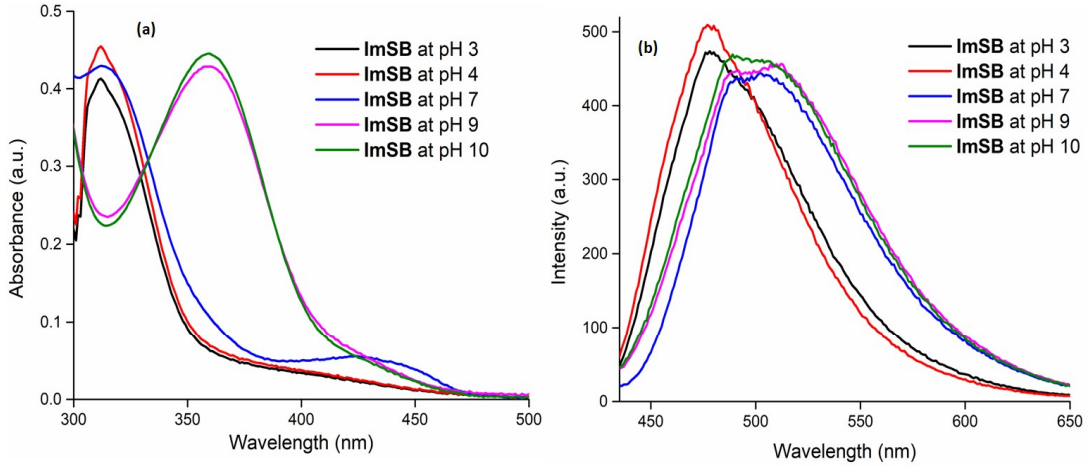

Figure 5.22 (**a**) UV-visible and (**b**) fluorescence response of **ImSB** under different pH

5.2.3 Sensing properties of ImSB

The sensing behaviour of **ImSB** was initially evaluated by the naked eye and under a UV lamp. An equimolar solutions of **ImSB** (10 μM) were added to a solutions of different metal ions (Na^+, K^+, Ag^+, Mg^{2+}, Ca^{2+}, Mn^{2+}, Co^{2+}, Fe^{2+}, Ni^{2+}, Cu^{2+}, Zn^{2+}, Cd^{2+}, Hg^{2+}, Pb^{2+}, Al^{3+}, Cr^{3+}, Fe^{3+}, La^{3+}, Eu^{3+}, Gd^{3+} and Yb^{3+}) in water buffered with HEPES (0.02 mM solution at pH 7.4). No colour change was observed for all the metal ions in the visible region, while bluish fluorescence under 365 nm UV lamp was observed for Al^{3+} (**Figure 5.23**).

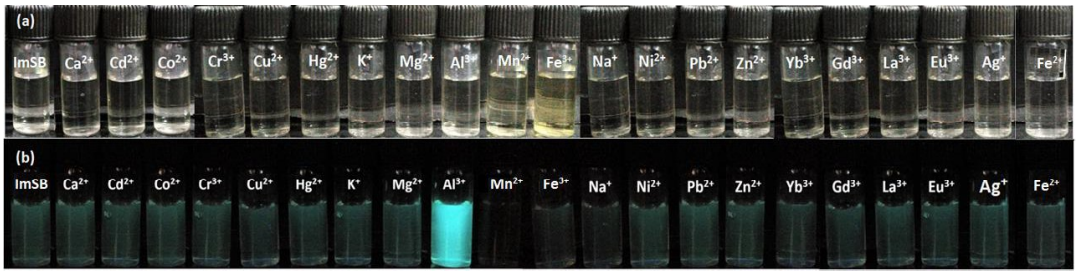

Figure 5.23 Visual colour change observed with the addition of different metal ions to **ImSB** (a) in natural light and (b) under 365 nm UV lamp

The UV-visible spectra of **ImSB** with different metal ions exhibited no effect on the absorption pattern of **ImSB**, while one new absorption band was observed for Cu^{2+}, Fe^{3+}, and Al^{3+} at λ_{max} = 416 nm, 398 nm, and 409 nm, respectively (**Figure 5.24a**). In the fluorescence spectra, on the addition of Al^{3+}, the emission peak at λ_{em} = 477 nm (Φ = 0.01) was red-shifted to 490 nm (Φ = 0.49) with increased fluorescence intensity (**Figure 5.24b**). A red-shifted peak at λ_{em} = 516 nm was observed on the addition of Zn^{2+} but with a slight change in the emission intensity. Upon complexation of **ImSB** with Al^{3+}, the drastic increase in fluorescence intensity is due to retardation of C=N isomerization and inhibition of PET [66-67].

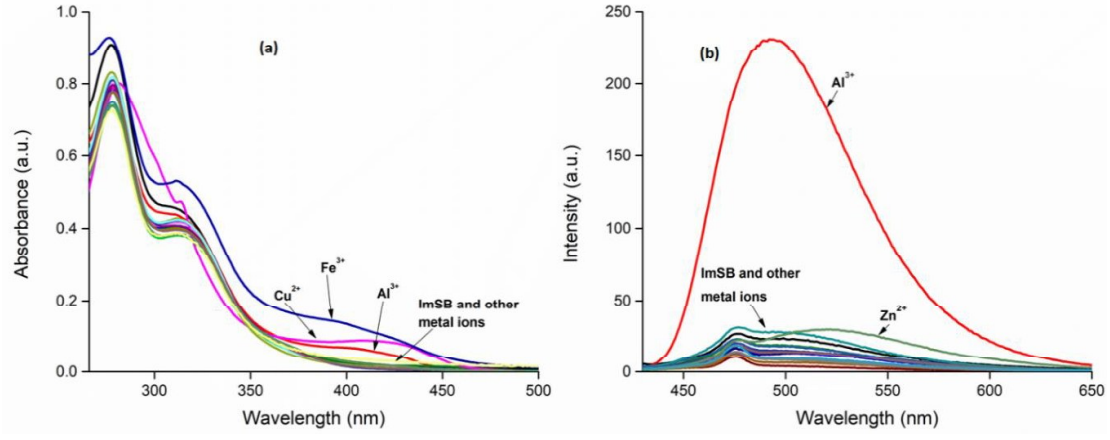

Figure 5.24 (**a**) UV-visible and (**b**) emission spectra (λ_{ex} = 410 nm) of **ImSB** (10 μM) upon addition of 1 equiv. of different metal ions

The fluorescence intensity of **ImSB**-Al^{3+} was not affected by presence of other interfering metal ions such as Na^{+}, K^{+}, Ag^{+}, Mg^{2+}, Ca^{2+}, Mn^{2+}, Co^{2+}, Fe^{2+}, Ni^{2+}, Cu^{2+}, Zn^{2+}, Cd^{2+}, Hg^{2+}, Pb^{2+}, Al^{3+}, Cr^{3+}, Fe^{3+}, La^{3+}, Eu^{3+}, Gd^{3+} and Yb^{3+}. The chemosensor **ImSB** responded selectively to Al^{3+} but a slight decrease in fluorescence emission was observed on the addition of Cu^{2+} and Fe^{3+} (**Figure 5.25a**). The presence of different interfering anions F^{-}, Cl^{-}, Br^{-}, I^{-}, HSO_4^{-}, SO_4^{-}, CH_3COO^{-} did not show any major effect on the fluorescence intensity (**Figure 5.25b**). Thus, **ImSB** can be used as an efficient and selective fluorescent chemosensor for Al^{3+} detection in the presence of most of the interfering metal ions and anions in the aqueous medium.

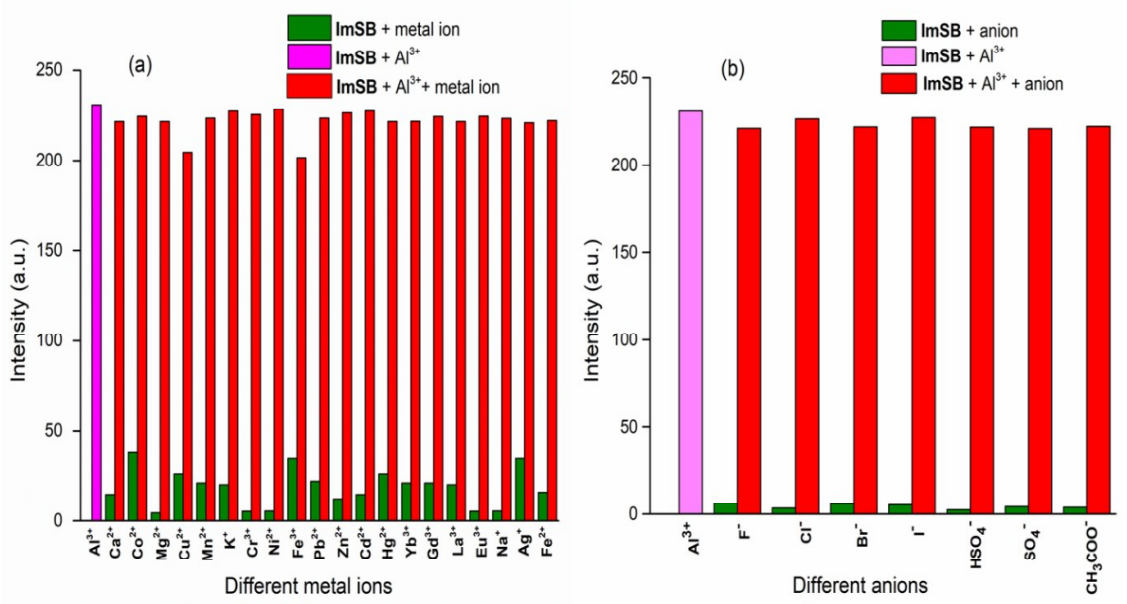

Figure 5.25 Selectivity of **ImSB (**10 μM**)** towards Al^{3+} in the presence of different (**a**) metal ions and (**b**) anions

The absorbance and fluorescence spectra of chemosensor **ImSB** were measured in the presence of Al^{3+} at different pH (**Figure 5.26**). The presence of absorption bands at λ_{max} = 312 nm, 402 nm and increase in fluorescence intensity at λ_{em} = 490 nm between pH 3-7 supported the existence of **ImSB**-Al^{3+} species (**Figure 5.26a**). These studies suggested that the complex is more stable at pH 7 and the stability decreases at higher pH due to the coordination of hydroxyl groups with Al^{3+}, while at lower pH due to the protonation of the nitrogen atom of **ImSB** (**Figure 5.26b**) [68].

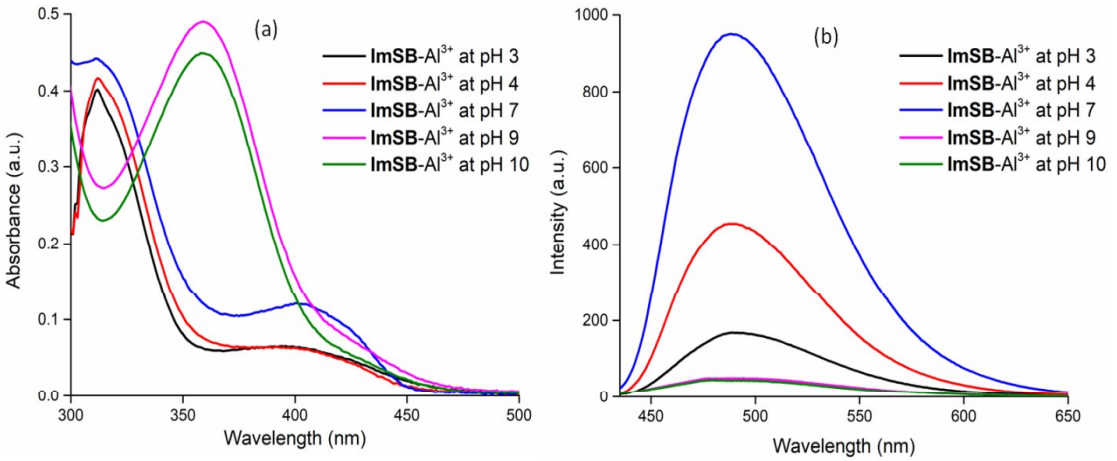

Figure 5.26 (**a**) UV-visible and (**b**) fluorescence response of **ImSB**-Al^{3+} under different pH

To further understand the mechanism of the turn-on fluorescence behaviour of **ImSB** toward Al^{3+} ion, fluorescence lifetime measurements were performed (**Figure 5.27**). The fluorescence lifetime of **ImSB** was very low (0.172 ns) in comparison to **ImSB**-Al^{3+} (2.996 ns).

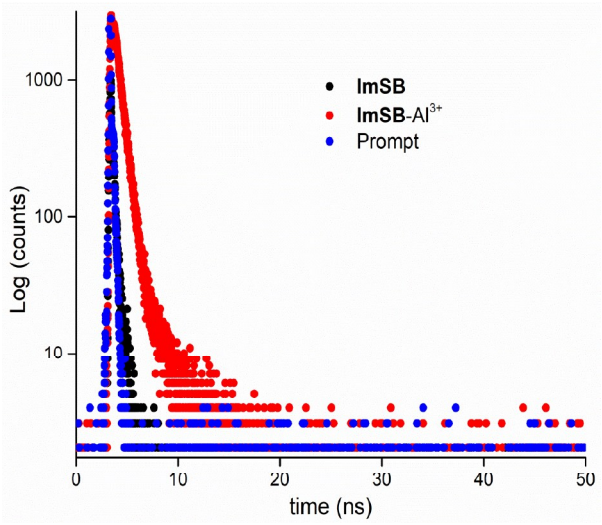

Figure 5.27 Time-resolved fluorescence decay of **ImSB** in absence and presence of Al^{3+}

The radiative (k_r) and non-radiative (k_{nr}) decay rate constants were computed using the equations, $\tau^{-1} = k_r + k_{nr}$ and $k_r = \Phi/\tau$. After complex formation, the value of k_r increases and k_{nr} decreases due to the rigidity in the complex in comparison to the free **ImSB** (**Table 5.3**).

Table 5.3 Fluorescence lifetime measurement data of **ImSB** and **ImSB**-Al^{3+} in solution

Entry	**Φ**	**τ_{avg} (ns)**	**k_r** ($\times 10^9$ S^{-1})	**k_{nr}** ($\times 10^9$ S^{-1})	**χ^2**
ImSB	0.01	0.172	0.058	5.755	0.816
ImSB-Al^{3+}	0.49	2.996	0.163	0.171	1.253

5.2.4 Binding behaviour studies

The binding of the **ImSB**-Al^{3+} complex was studied using different spectroscopic techniques. On addition of 1 equiv. of Al^{3+}, the absorption (**Figure 5.28a**) and emission intensities (**Figure 5.28b**) became steady indicating the coordination of **ImSB** with Al^{3+} in 1:1 binding mode.

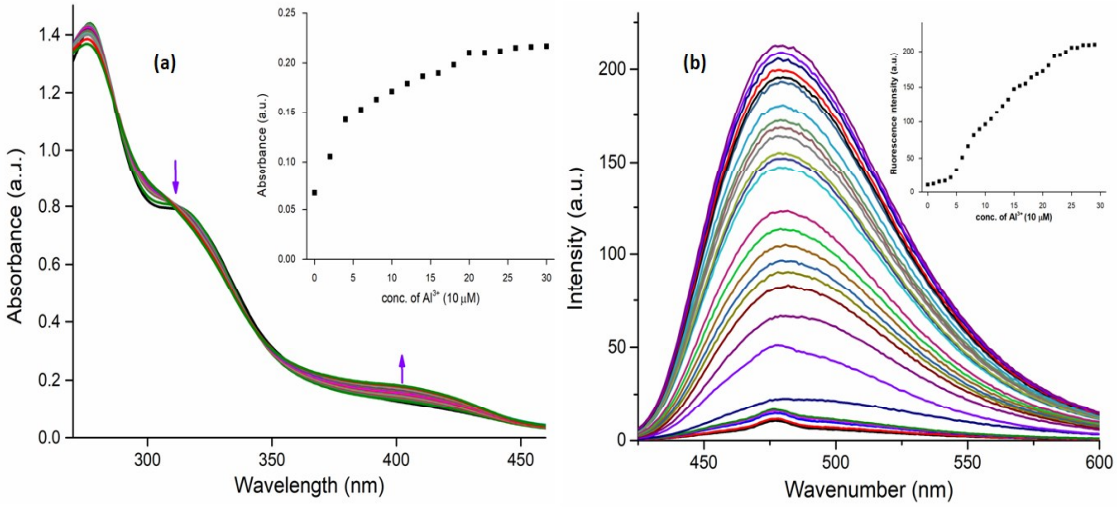

Figure 5.28 (**a**) UV-visible and (**b**) emission spectra of **ImSB** in the presence of a varying amount of Al^{3+}; inset: line graph of absorbance and emission intensities of **ImSB** depending on the concentrations of Al^{3+}

Job's plots obtained from the fluorescence data also showed 1:1 stoichiometry for the complexation of Al^{3+} with **ImSB** (**Figure 5.29a**). The binding constant (K_B) evaluated from the fluorescence titration data using the Benesi-Hildebrand plot was 4.16 x 10^6 M^{-1}, indicating efficient binding of **ImSB** with Al^{3+} (**Figure 5.29b**).

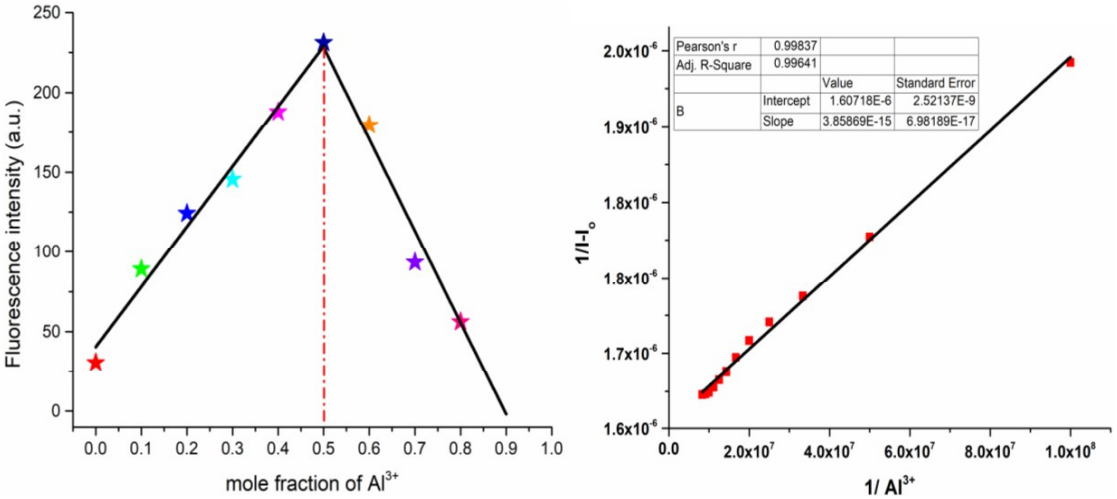

Figure 5.29 (**a**) Job′s plot and (**b**) Benesi-Hildebrand plot of **ImSB** vs Al^{3+} titration

The detection limit (DL) of **ImSB** for Al^{3+} was 54 nM and was determined using the equation, [22] DL = 3σ/k, where σ is the standard deviation of blank measurements; k is the slope of intensity versus sample concentration (**Figure 5.30**).

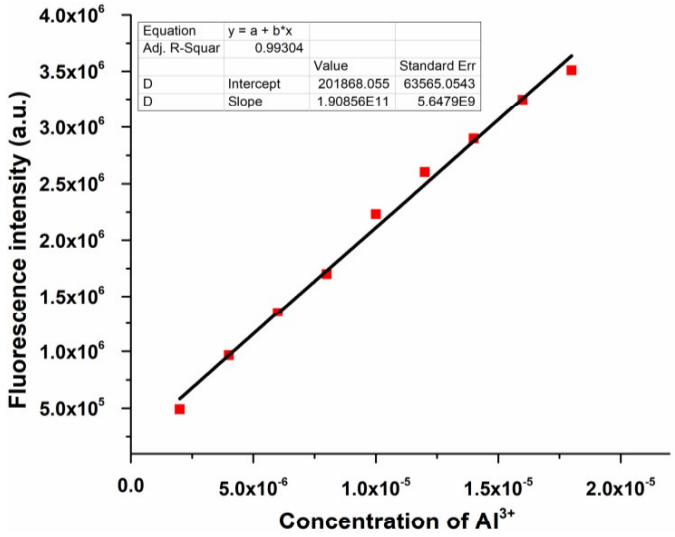

Figure 5.30 Detection limit calculation plot

In the IR spectra, a broad peak at 3344 cm^{-1} disappeared, a peak at 1581 cm^{-1} due to $\nu_{(C=N)}$ stretching appeared, a peak due to azomethine group of quinoline ring shifted to 1512 cm^{-1} and a peak at 1404 cm^{-1} appeared due to $\nu_{(NO_3^-)}$ after complexation (**Figure 5.31a**). In the ^1H NMR spectra of **ImSB**-Al^{3+}, the shifting of imine protons signals to 9.53 ppm (H_a) and 8.95 ppm (H_b), the disappearance of phenolic -OH (H_c) signal indicate binding of Al^{3+} with **ImSB** (**Figure 5.31b**).

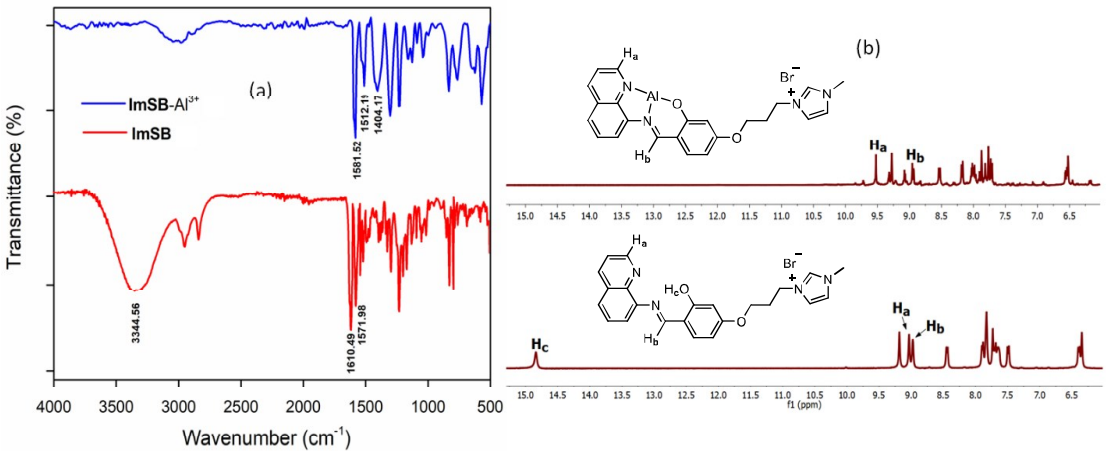

Figure 5.31 (**a**) IR (solid- state) and (**b**) ^1H NMR spectra of **ImSB** and **ImSB**-Al^{3+} (DMSO-d_6)

The ESI-MS analysis showed a peak at 537.17, due to [**ImSB** + Al + $2NO_3$ - Br]$^+$ (537.13, calculated), which also supported 1:1 stoichiometry for the **ImSB**-Al^{3+} complex (**Figure 5.32**).

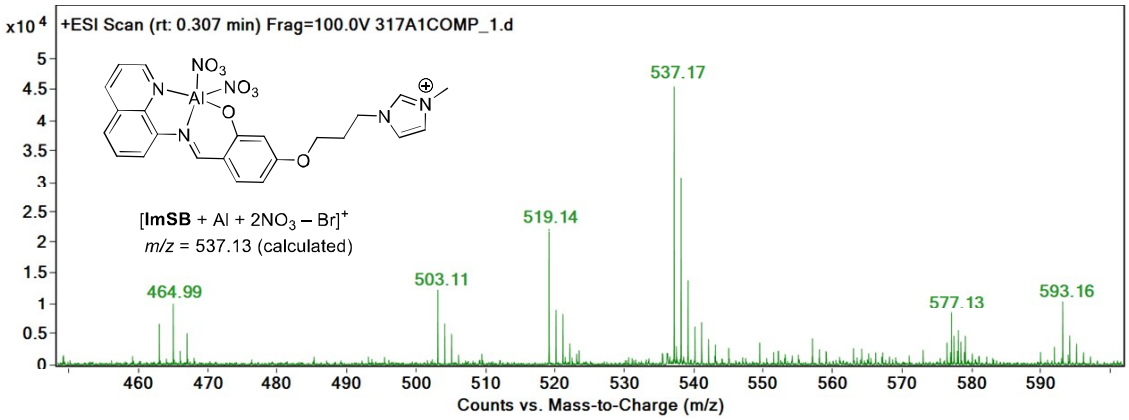

Figure 5.32 Mass spectrum of **ImSB**-Al^{3+}

5.2.5 Reversibility of chemosensor ImSB

The reversibility of the chemosensor **ImSB** was tested using strong chelating agent EDTA. Titration experiments revealed that increasing the concentration of EDTA (0.0-2.0 equiv.) to a solution of **ImSB**-Al^{3+} showed a gradual decrease in the fluorescence intensity at λ_{em} = 490 nm, which indicates that **ImSB**-Al^{3+} complex breaks and EDTA binds with Al^{3+}, leaving uncomplexed **ImSB** (**Figure 5.33a**). The reaction was completed within 5 min after the addition of EDTA, showing the rapid capture of Al^{3+}. A reversibility chart constructed with the sequential addition of Al^{3+} and EDTA to the aqueous solutions of **ImSB** suggesting reversible nature of **ImSB** up to five cycles with a gradual decrease in efficiency (**Figure 5.33b**).

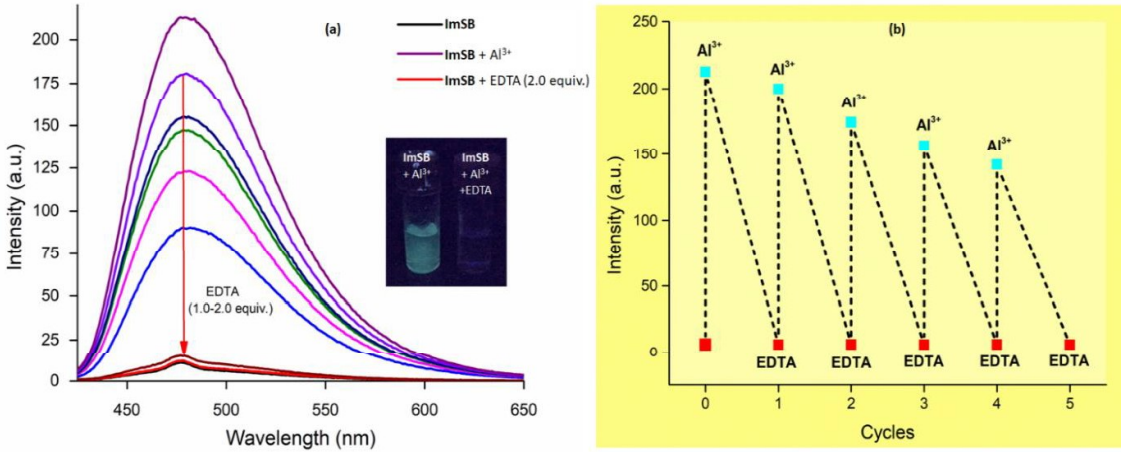

Figure 5.33 (**a**) Fluorescence spectra of **ImSB** in the presence of Al^{3+} and EDTA (0.0-2.0 equiv.) (**b**) Reversibility chart of **ImSB** after sequential addition of Al^{3+} and EDTA

5.2.6 Theoretical studies

Geometry optimization of **ImSB** (keto and enol forms), **ImSB**$^{+}$ (without Br^{-}), **ImSB**-$Al(NO_3)_2$, and **ImSB**$^{+}$-$Al(NO_3)_2$ (without Br^{-}) was performed using DFT/B3LYP method. Since the crystal structure of **ImSB** is obtained in keto form, therefore the bond lengths and bond angles were compared with optimized keto structure (**Figure 5.34a** and **b**).

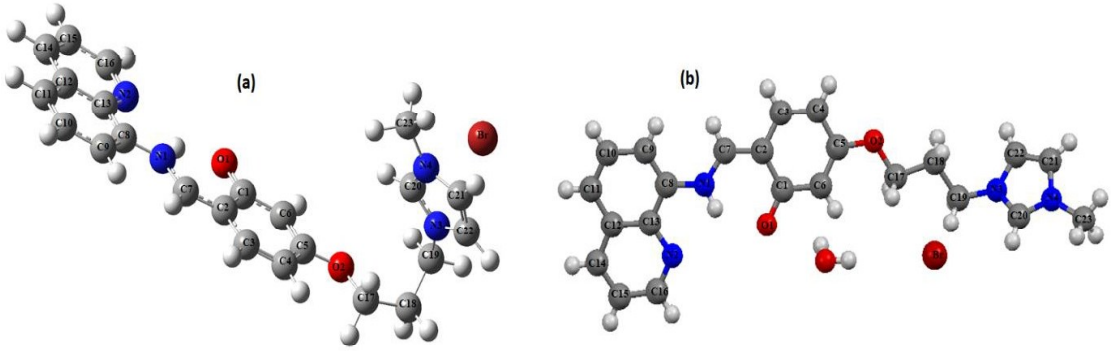

Figure 5.34 (a) DFT optimized structure of keto form and (b) crystal structure of **ImSB**

These results showed that the calculated values are slightly larger than experimental values due to the intermolecular interactions present in the crystal, which are absent in the isolated state used for theoretical calculation. The largest difference in bond angle is observed between atoms O(2)-C(5)-C(6), O(2)-C(5)-C(4), and C(17)-C(18)-C(19) (**Table 5.4**).

Table 5.4 Comparison between some selected geometrical parameters of **ImSB** (keto form) by single crystal XRD and theoretical calculations

Parameters	**XRD**	**Calculated**
Bond length		
O(1)–C(1)	1.2779(16)	1.25930
O(2)–C(5)	1.3595(15)	1.37367
O(2)–C(17)	1.4255(16)	1.42885
N(1)–C(8)	1.4075(16)	1.40145
N(1)–C(7)	1.3241(17)	1.33343
N(4)–C(21)	1.3811(17)	1.38468
N(4)–C(20)	1.3279(17)	1.33784
N(4)–C(23)	1.4708(17)	1.47687
N(3)–C(19)	1.4709(16)	1.47010
N(3)–C(22)	1.3862(16)	1.38711
N(3)–C(20)	1.3325(17)	1.34238
C(21)–C(22)	1.3566(18)	1.36602
C(7)–C(2)	1.3927(17)	1.39543

C(2)–C(1)	1.4541(17)	1.47554
C(2)–C(3)	1.4276(18)	1.42672
C(1)–C(6)	1.4311(17)	1.43995
C(19)–C(18)	1.5221(19)	1.53586
C(6)–C(5)	1.3767(18)	1.37544
N(2)–C(13)	1.3663(16)	1.35855
N(2)–C(16)	1.3186(18)	1.31908
C(8)–C(13)	1.4300(18)	1.43632
C(8)–C(9)	1.3788(17)	1.38597
C(4)–C(5)	1.4249(18)	1.43397
C(18)–C(17)	1.5182(18)	1.52495
Bond angle		
C(5)–O(2)–C(17)	117.11(10)	120.24763
C(7)–N(1)–C(8)	125.28(11)	127.20193
C(21)–N(4)–C(23)	126.12(11)	125.02697
C(20)–N(4)–C(21)	108.53(11)	109.21709
C(20)–N(4)–C(23)	125.31(12)	125.75498
C(22)–N(3)–C(19)	126.25(11)	126.35761
C(20)–N(3)–C(19)	124.85(11)	125.47373
C(20)–N(3)–C(22)	108.90(11)	108.05887
C(16)–N(2)–C(13)	117.00(12)	118.35100
N(1)–C(8)–C(13)	115.90(11)	116.25799
N(1)–C(7)–C(2)	124.33(12)	124.07009
C(7)–C(2)–C(1)	121.67(12)	120.85822
C(7)–C(2)–C(3)	118.33(11)	119.38750
C(3)–C(2)–C(1)	120.00(11)	119.75395
O(1)–C(1)–C(6)	121.71(11)	122.51688
N(3)–C(19)–C(18)	111.63(11)	112.87054
O(2)–C(5)–C(6)	**124.64(12)**	**115.97064**
O(2)–C(5)–C(4)	**113.30(11)**	**122.04984**
C(17)–C(18)–C(19)	**107.99(11)**	**113.55552**
O(2)–C(17)–C(18)	107.27(11)	107.26271

The optimized structures of the enolic **ImSB** (a) and its **ImSB**-$Al(NO_3)_2$ (b) complex are shown in **Figure 5.35**. Photophysical studies revealed that complexation takes place between the enolic form of **ImSB** and Al^{3+}, therefore some selected bond distance and bond angle values of optimized geometries are listed in **Table 5.5**. Upon complex formation, significant changes in the C(1)-O(1), C(7)-N(1), and N(2)-C(13) bond distances were observed and calculated Al-O/Al-N distances are in the range of 1.824-2.054 Å.

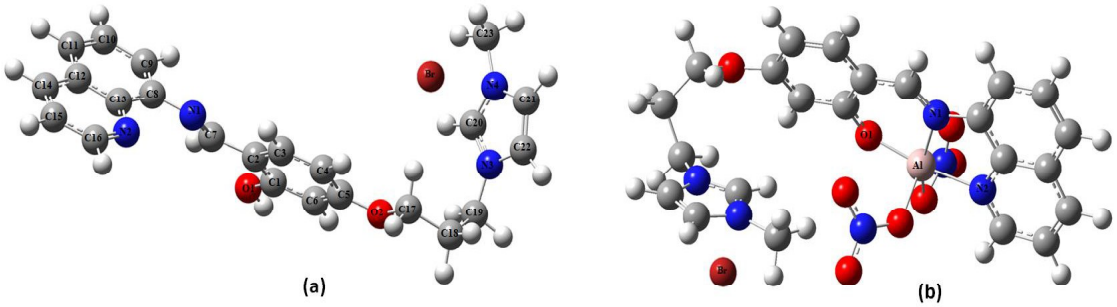

Figure 5.35 DFT optimized structures of (a) **ImSB** (enol form) and (b) **ImSB**-$Al(NO_3)_2$

Table 5.5 Selected bond lengths (Å) and bond angles (°) of DFT optimized structure of **ImSB** and its aluminium complex

Parameters	**ImSB (enol) (Calculated values)**	**Aluminium complex (Calculated values)**
Bond lengths		
C(1)–O(1)	1.354	1.364
C(7)–N(1)	1.278	1.316
N(1)–C(8)	1.396	1.411
N(2)–C(13)	1.361	1.367
N(2)–C(16)	1.319	1.328
Al–O(1)	-	1.824
Al–N(1)	-	2.008
Al–N(2)	-	2.054
Bond angles		
O(1)–C(1)–C(2)	117.66	122.67
C(2)–C(7)–N(1)	122.93	125.69
C(7)–N(1)–C(8)	119.17	122.03
N(1)–C(8)–C(13)	119.06	114.05
N(2)–Al–N(1)	-	80.60
N(1)–Al–O(1)	-	92.12

In the ground state, the electron density of **ImSB**$^+$ in both HOMO and LUMO is distributed over the entire molecule excluding the alkyl chain and imidazole ring**.** In the complex, the electron density in HOMO mainly resides on the phenolic part to half of the quinoline moiety and in LUMO it is primarily distributed over the quinoline part (**Figure 5.36**). The HOMO and LUMO energies of **ImSB**$^+$ are less stabilized (3.908 eV) than its aluminium complex **ImSB**$^+$-$Al(NO_3)_2$ (3.377 eV) therefore the formation of the complex is more feasible due to

the narrowing of energy gap (0.531 eV) between HOMO and LUMO. This reduced energy gap also justifies the appearance of a new absorption band at (λ_{max} = 409 nm).

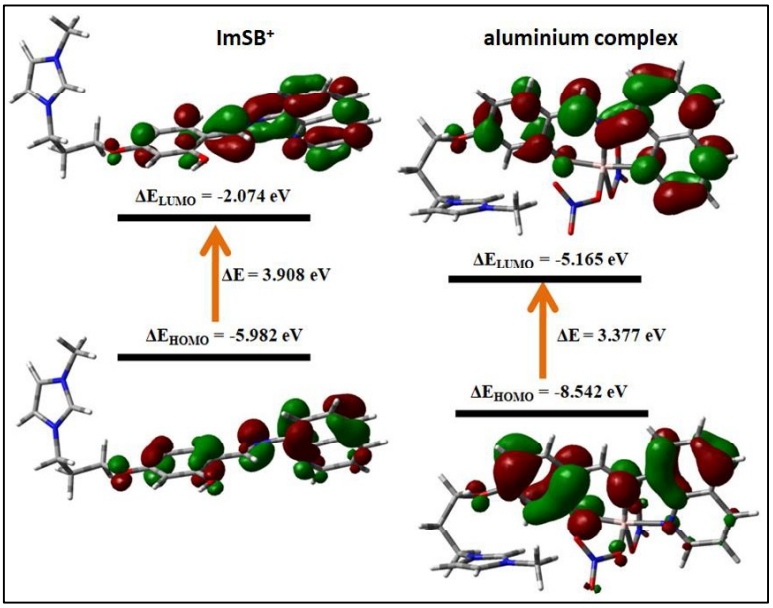

Figure 5.36 Energy level diagram of **ImSB** and its aluminium complex **ImSB**$^{+}$-Al$(NO_3)_2$

To study the electronic transitions, TDDFT calculations were performed. The lowest 20 singlet-singlet transitions are computed and TDDFT results are in good agreement with the experimental results. Energies of a few selected frontier molecular orbital and main electronic transitions are given in **Figure 5.37** and **Figure 5.38**.

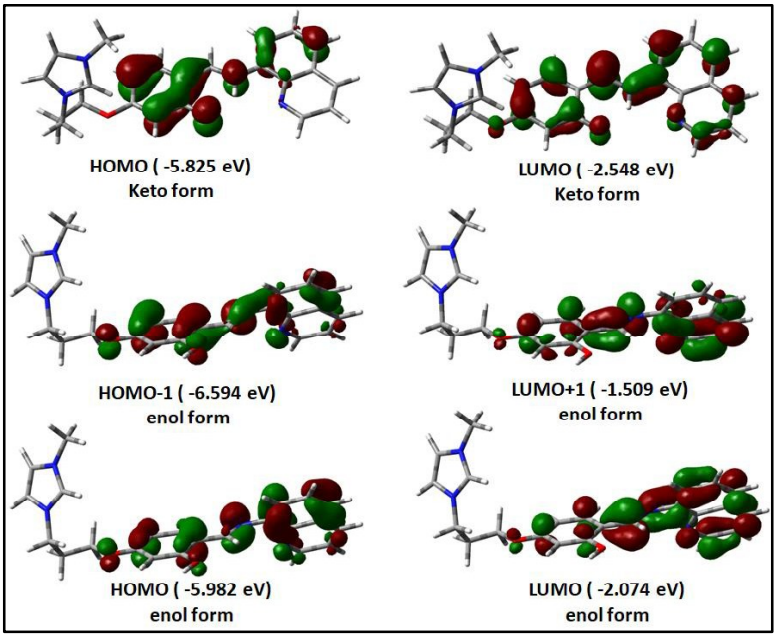

Figure 5.37 Energy of selected frontier molecular orbitals of **ImSB**$^{+}$

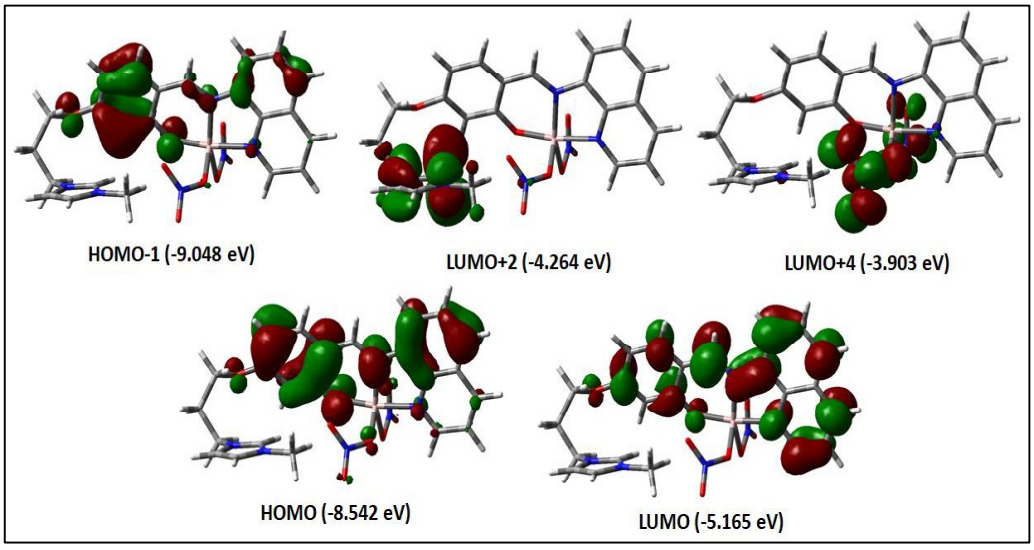

Figure 5.38 Energy of selected frontier molecular orbitals of aluminium complex

In **ImSB**$^+$ the absorption bands at 435 nm (keto form), 309 nm (enol form), and 279 nm (both keto and enol forms) are assigned to HOMO→LUMO, HOMO-1→LUMO, and HOMO-1→LUMO+2 transitions, respectively (**Figure 5.39**). In aluminium complex, **ImSB**$^+$-$Al(NO_3)_2$ the absorption bands at 418 nm, 308 nm, and 270 nm are due to HOMO→LUMO, HOMO-1→ LUMO+2, and HOMO→LUMO+4 transitions, respectively (**Figure 5.40**).

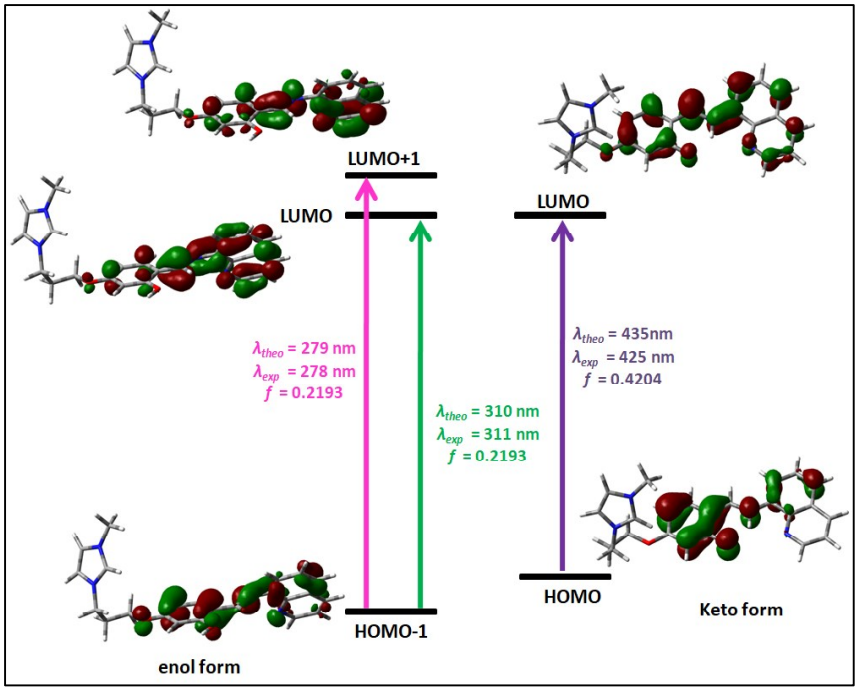

Figure 5.39 Pictorial representation of key transitions involved in the UV-visible spectra of **ImSB**$^+$

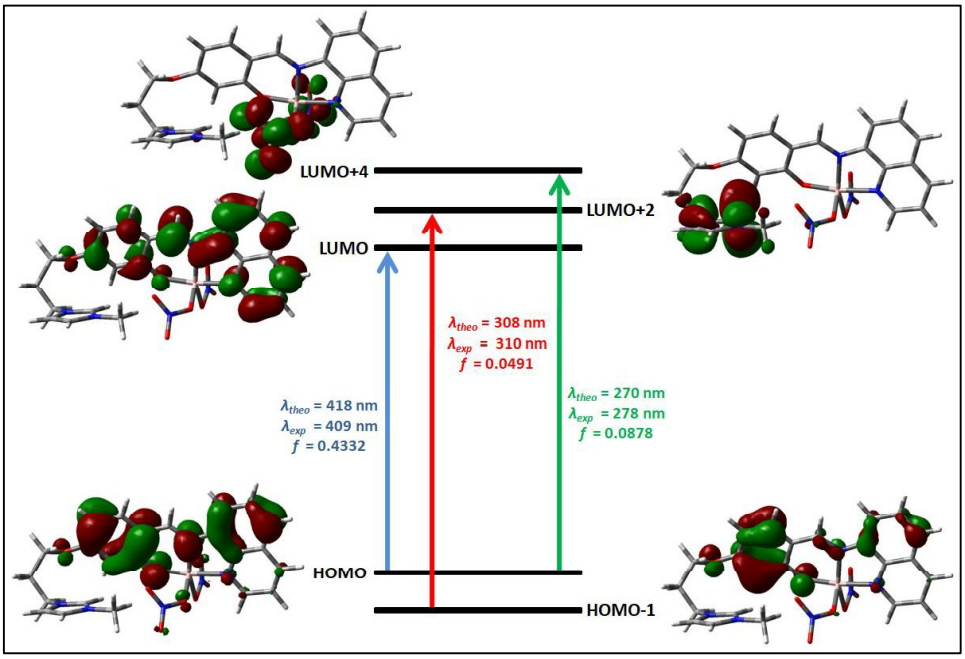

Figure 5.40 Pictorial representation of key transitions involved in the UV-visible spectra of aluminium complex

5.2.7 Real sample analysis

The efficiency and sensitivity of **ImSB** were evaluated on mineral, river, and tap water samples. The bottled mineral water was purchased from the local market, the environmental water sample was obtained from the Ganga River (Rishikesh, India) and the tap water sample was taken from our laboratory. The water samples were filtrated, centrifuged for 10 min, and spiked with standard Al^{3+} solution. **ImSB** was added to detect Al^{3+} and satisfactory recovery values are obtained (**Table 5.6**). Each experiment was repeated three times. The presence of Cu^{2+} and Fe^{3+} concomitant ions in the river and tap water samples may be a reason affecting the recovery of Al^{3+}.

Table 5.6 Recovery study of spiked Al^{3+} in water samples

Sample	**Al^{3+} spiked (μM)**	**Al^{3+} recovered, mean ± standard deviation (SD) (μM)**	**Recovery (%)**
Mineral water	20	19.97 ± 0.35	99.85
River water	20	19.54 ± 0.02	97.73
Tap water	20	19.59 ± 0.14	97.99

5.2.8 Comparison of ImSB with some of the previously reported Al^{3+} chemosensors

A comparison of **ImSB** with different chemosensor based on Schiff bases reported in the literature is shown in **Table 5.7**. **ImSB** shows a lower detection limit, a high binding constant for Al^{3+} in green solvent water and is also applicable to real water sample analysis.

Table 5.7 A comparative study of **ImSB** with some literature reported chemosensors for Al^{3+} detection

Solvent system	Detection limit	Binding constant	Real sample analysis	Reference
Ethanol	0.214 μM	6.07 x 10^3 M^{-1}	NA	[69]
Methanol	12.4 μM	4.72 x 10^4 M^{-1}	NA	[70]
Methanol-H_2O	4.32 μM	2.1 x 10^4 M^{-1}	NA	[71]
Methanol-Tris	0.178 μM	5.49 x 10^4 M^{-1}	River and tap water	[72]
DMF-H_2O	6.7 μM	3.21 x 10^6 M^{-1}	NA	[66]
DMF	200 nM	3.42 x 10^3 M^{-1}	NA	[68]
Methanol	93 nM	3.59 x 10^5 M^{-1}	NA	[73]
DMSO-H_2O	NA	4.03 x 10^4 M^{-1}	NA	[74]
Ethanol-H_2O	0.11 μM	7.033 x 10^3 M^{-1}	NA	[75]
DMSO-H_2O	0.6 μM	1 x 10^5 M^{-1}	NA	[76]
H_2O	54 nM	4.16 x 10^6 M^{-1}	River, tap and mineral water	Present work

5.3 Experimental

5.3.1 Synthesis of imidazolium-based Schiff base chemosensor (ImSB)

To a stirred solution of **ImA** (discussed in chapter 2, section 2.4) (0.500 g, 1 mmol) in ethanol (10 mL), 8-aminoquinoline (0.276 g, 1 mmol) was added. This mixture was stirred for 5 h under reflux, the solvent was removed under reduced pressure and a viscous brown liquid was obtained. The crude product was further washed with ethyl acetate and diethyl ether several times and **ImSB** precipitated as bright yellow solid was dried under vacuum (**Scheme 5.1**).

5.3.2 Physical and spectral data of ImSB

Imidazolium-based Schiff base (ImSB):

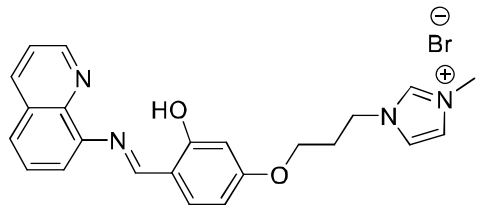

Bright Yellow solid (89%); mp: 109-110°C; FTIR/cm^{-1}: 3344.56, 1610.49, 1571.98; ^{1}H NMR (400 MHz, DMSO-d_6) δ 14.84 (s, 1H), 9.19 (s, 1H), 9.04 (s, 1H), 8.98 (dd, J = 4.0, 1.5 Hz, 1H), 8.45 (d, J = 8.3 Hz, 1H), 7.89 (d, J = 8.0 Hz, 1H), 7.86-7.82 (m, 2H), 7.73 (s, 1H), 7.70 (d, J = 7.9 Hz, 1H), 7.65 (dt, J = 8.3, 4.3 Hz, 1H), 7.49 (d, J = 8.8 Hz, 1H),6.39 (dd, J = 8.7, 2.3 Hz, 1H), 6.35 (d, J = 2.2 Hz, 1H), 4.37 (t, J = 6.8 Hz, 2H), 4.10 (t, J = 5.8 Hz, 2H), 3.86 (s, 3H), 2.30 (p, J = 6.3 Hz, 2H); ^{13}C NMR (100 MHz, DMSO-d_6) δ 169.0, 164.1, 160.9, 150.9, 142.6, 141.4, 137.2, 136.8, 135.0, 129.1, 127.3, 126.2, 124.0, 122.9, 122.7, 117.4, 113.5, 107.8, 102.3, 65.3, 46.8, 36.2, 29.3. HRMS (ESI): *m/z* calcd for $[C_{23}H_{23}N_4O_2]^+$ [**ImSB** - Br]$^+$ 387.1816, found 387.1824.

5.4 Conclusions

In present work, a highly water-soluble imidazolium-based quinoline Schiff base **ImSB** was synthesized and its fluorescence properties were explored. In solid-state, **ImSB** was obtained as yellow solid in its keto form, and formation of J-aggregated structure is the reason for strong yellow fluorescence. In polar protic solvents, **ImSB** was found in both keto and enol forms while in polar aprotic solvent enol form was predominant. In aqueous medium, the keto form was found at higher concentration while enol form was present at a lower concentration of **ImSB**. It selectively monitored Al^{3+} with an increase in fluorescence intensity exhibiting fluorescence turn-on behaviour. In aqueous medium, **ImSB** exhibited weak fluorescence due to PET and C=N isomerization which was suppressed efficiently on adding Al^{3+}. The low detection limit (54 nM), strong binding constant (4.16 x 10^6 M^{-1}), least interference by other ions are among the few advantages of **ImSB**. Moreover, the hydrophilic imidazolium-based unit facilitates solubility in water that aids to perform the chemosensing in aqueous medium. The increased value of quantum yield (Φ = 0.49) and fluorescence lifetime (τ = 2.996 ns) indicate enhanced rigidity in **ImSB** after coordination with Al^{3+}. **ImSB** was also used for detecting Al^{3+} in real water samples and promising results were obtained. Some important experimental results are corroborated by DFT and TDDFT calculations.

5.5 References

[1] Nayim, S. M. T. I.; Hasan, M. Z.; Seth, P. P.; Gupta, P.; Thakur, S.; Kumar, D.; Jamwal, A. *Materials Today: Proceedings* **2020**, *21*, 1421-1424.

[2] Wang, Y.; Ma, Z.-Y.; Zhang, D.-L.; Deng, J.-L.; Chen, X.; Xie, C.-Z.; Qiao, X.; Li, Q.-Z.; Xu, J.-Y. *Spectrochimica Acta Part A: Molecular and Biomolecular Spectroscopy* **2018**, *195*, 157-164.

[3] Kumar, V.; Kumar, A.; Diwan, U.; Shweta; Ramesh; Srivastava, S. K.; Upadhyay, K. K. *Sensors and Actuators B: Chemical* **2015**, *207*, 650-657.

[4] Sadak, A. E.; Karakuş, E. *Journal of Fluorescence* **2020**, *30*, 213-220.

[5] Nejad, H. H.; Ordoee, B.; Khanmohammadi, M. *Journal of Molecular Structure* **2019**, *1196*, 861-865.

[6] Sukharenko, E. V.; Samoylova, I. V.; Nedzvetsky, V. S. *Regulatory Mechanisms in Biosystems* **2017**, *8*, 461-467.

[7] Gupta, N.; Gaurav, S. S.; Kumar, A. *American Journal of Plant Sciences* **2013**, *4*, 21-37.

[8] Exley, C. *Environmental Science: Processes & Impacts* **2013**, *15*, 1807-1816.

[9] Exley, C.; House, E. R. *Monatshefte für Chemie - Chemical Monthly* **2011**, *142*, 357-363.

[10] Mondal, S.; Bhanja, A. K.; Ojha, D.; Mondal, T. K.; Chattopadhyay, D.; Sinha, C. *RSC Advances* **2015**, *5*, 73626-73638.

[11] Li, S. Y.; Zhang, D. B.; Wang, J. Y.; Lu, R. M.; Zheng, C. H.; Pu, S. Z. *Sensors and Actuators B: Chemical* **2017**, *245*, 263-272.

[12] Kong, D.; Yan, F.; Luo, Y.; Ye, Q.; Zhou, S.; Chen, L. *Analytica Chimica Acta* **2017**, *953*, 63-70.

[13] Wu, D.; Sedgwick, A. C.; Gunnlaugsson, T.; Akkaya, E. U.; Yoon, J.; James, T. D. *Chemical Society Reviews* **2017**, *46*, 7105-7123.

[14] Gale, P. A.; Caltagirone, C. *Coordination Chemistry Reviews* **2018**, *354*, 2-27.

[15] Magri, D. C. *Analyst* **2015**, *140*, 7487-7495.

[16] Wu, J.; Liu, W.; Ge, J.; Zhang, H.; Wang, P. *Chemical Society Reviews* **2011**, *40*, 3483-3495.

[17] Ding, Y.; Tang, Y.; Zhu, W.; Xie, Y. *Chemical Society Reviews* **2015**, *44*, 1101-1112.

[18] In, B.; Hwang, G. W.; Lee, K.-H. *Bioorganic & Medicinal Chemistry Letters* **2016**, *26*, 4477-4482.

[19] Yeap, G.-Y.; Chan, Y.-H.; Mahmood, W. A. K. *Journal of Fluorescence* **2017**, *27*, 2017-2022.

[20] Gupta, V. K.; Shoora, S. K.; Kumawat, L. K.; Jain, A. K. *Sensors and Actuators B: Chemical* **2015**, *209*, 15-24.

[21] Bartwal, G.; Aggarwal, K.; Khurana, J. M. *New Journal of Chemistry* **2018**, *42*, 2224-2231.

[22] Naskar, B.; Das, K.; Mondal, R. R.; Maiti, D. K.; Requena, A.; Cerón-Carrasco, J. P.; Prodhan, C.; Chaudhuri, K.; Goswami, S. *New Journal of Chemistry* **2018**, *42*, 2933-2941.

[23] Wang, F.; Zeng, X.; Zhao, X.; Lu, H.; Wang, Q. *Journal of Luminescence* **2019**, *208*, 302-306.

[24] Balamurugan, G.; Velmathi, S.; Thirumalaivasan, N.; Wu, S. P. *Analyst* **2017**, *142*, 4721-4726.

[25] Liu, Z. C.; Zhu, W. P.; Chen, Y. H.; Li, Y. X.; Ding, Y. J.; Yang, W. J.; Li, K. *Dalton Transactions* **2015**, *44*, 16528-16533.

[26] Liu, Z.; Ren, K.; Chen, Y.; Li, Y.; Xie, J.; Ding, Y.; Li, L.; Li, K.; Zhu, W.; Yang, W.; Xu, Z. *RSC Advances* **2017**, *7*, 38160-38165.

[27] Berhanu, A. L.; Gaurav; Mohiuddin, I.; Malik, A. K.; Aulakh, J. S.; Kumar, V.; Kim, K.-H. *TrAC Trends in Analytical Chemistry* **2019**, *116*, 74-91.

[28] Pan, Z.-H.; Zhou, J.-W.; Luo, G.-G. *Physical Chemistry Chemical Physics* **2014**, *16*, 16290-16301.

[29] Bhowon, M. G.; Jhaumeer Laulloo, S.; Hosten, E. C.; Khodabaccus, M. M.; Rhyman, L.; Ramasami, P. *Journal of Molecular Structure* **2019**, *1175*, 13-23.

[30] Cheng, J.; Ma, X.; Zhang, Y.; Liu, J.; Zhou, X.; Xiang, H. *Inorganic Chemistry* **2014**, *53*, 3210-3219.

[31] Sousa, J.; Oliveira, D. R.; Lomonaco, D.; Correia, A. N.; Sousa, C. P.; de Lima Neto, P.; Paulo, T. F.; Mazzetto, S. E.; Clemente, C. S.; Mele, G. *Journal of Molecular Structure* **2019**, *1181*, 279-286.

[32] Alici, O.; Erdemir, S. *Sensors and Actuators B: Chemical* **2015**, *208*, 159-163.

[33] Anand, T.; Sivaraman, G.; Mahesh, A.; Chellappa, D. *Analytica Chimica Acta* **2015**, *853*, 596-601.

[34] Yan, L.-Q.; Ma, Y.; Cui, M.-F.; Qi, Z.-J. *Analytical Methods* **2015**, *7*, 6133-6138.

[35] Banerjee, S.; Brandão, P.; Saha, A. *RSC Advances* **2016**, *6*, 101924-101936.

[36] Shen, K.; Mao, S.; Shi, X.; Wang, F.; Xu, Y.; Aderinto, S. O.; Wu, H. *Luminescence* **2018**, *33*, 54-63.

[37] Das, B.; Dey, S.; Maiti, G. P.; Bhattacharjee, A.; Dhara, A.; Jana, A. *New Journal of Chemistry* **2018**, *42*, 9424-9435.

[38] Shweta; Neeraj; Asthana, S. K.; Mishra, R. K.; Upadhyay, K. K. *RSC Advances* **2016**, *6*, 55430-55437.

[39] Naskar, B.; Modak, R.; Sikdar, Y.; Maiti, D. K.; Bauzá, A.; Frontera, A.; Katarkar, A.; Chaudhuri, K.; Goswami, S. *Sensors and Actuators B: Chemical* **2017**, *239*, 1194-1204.

[40] Leng, X.; Xu, W.; Qiao, C.; Jia, X.; Long, Y.; Yang, B. *RSC Advances* **2019**, *9*, 6027-6034.

[41] Li, Q.-F.; Wang, J.-T.; Wu, S.; Ge, G.-W.; Huang, J.; Wang, Z.; Yang, P.; Lin, J. *Sensors and Actuators B: Chemical* **2018**, *259*, 484-491.

[42] Song, H.; Zhang, Z. *Dyes and Pigments* **2019**, *165*, 172-181.

[43] Kim, Y.-H.; Youk, J. S.; Moon, S. Y.; Choe, J.-I.; Chang, S.-K. *Chemistry Letters* **2004**, *33*, 702-703.

[44] Dai, C.-G.; Wang, J.-L.; Fu, Y.-L.; Zhou, H.-P.; Song, Q.-H. *Analytical Chemistry* **2017**, *89*, 10511-10519.

[45] Wei, T.; Wang, F.; Chen, Y.; Qiang, J.; Zhang, Z.; Chen, T.; Chen, X. *Dyes and Pigments* **2018**, *159*, 322-330.

[46] Zhang, Z.; Zou, Y.; Deng, C. *RSC Advances* **2017**, *7*, 14742-14751.

[47] Vongnam, K.; Muangnoi, C.; Rojsitthisak, P.; Sukwattanasinitt, M.; Rashatasakhon, P. *Biosensors and Bioelectronics* **2016**, *86*, 472-476.

[48] Sarkar, D.; Pramanik, A.; Jana, S.; Karmakar, P.; Mondal, T. K. *Sensors and Actuators B: Chemical* **2015**, *209*, 138-146.

[49] Guo, L.; Hong, S.; Lin, X.; Xie, Z.; Chen, G. *Sensors and Actuators B: Chemical* **2008**, *130*, 789-794.

[50] Li, Y.; Wu, J.; Jin, X.; Wang, J.; Han, S.; Wu, W.; Xu, J.; Liu, W.; Yao, X.; Tang, Y. *Dalton Transactions* **2014**, *43*, 1881-1887.

[51] Pedras, B.; Rosa, V.; Welter, R.; Lodeiro, C.; Avilés, T. *Inorganica Chimica Acta* **2012**, *381*, 143-149.

[52] Zhang, Y.; Guo, X.; Zheng, L.; Jia, L. *Journal of Luminescence* **2017**, *188*, 283-288.

[53] Roy, A.; Dey, S.; Roy, P. *Sensors and Actuators B: Chemical* **2016**, *237*, 628-642.

[54] Hazra, A.; Roy, A.; Mukherjee, A.; Maiti, G. P.; Roy, P. *Dalton Transactions* **2018**, *47*, 13972-13989.

[55] Huang, P.-C.; Fang, H.; Xiong, J.-J.; Wu, F.-Y. *Methods and Applications in Fluorescence* **2017**, *5*, 024014-024022.

[56] Al-Kindy, S. M. Z.; Al-Mafrigi, Z.; Shongwe, M. S.; Suliman, F. E. O. *Luminescence* **2011**, *26*, 462-470.

[57] Tian, X.; Qi, X.; Liu, X.; Zhang, Q. *Sensors and Actuators B: Chemical* **2016**, *229*, 520-527.

[58] Jeong, E.; Yoon, S.; Lee, H. S.; Kumar, A.; Chae, P. S. *Dyes and Pigments* **2019**, *162*, 348-357.

[59] Mezzetta, A.; Łuczak, J.; Woch, J.; Chiappe, C.; Nowicki, J.; Guazzelli, L. *Journal of Molecular Liquids* **2019**, *289*, 111155-111163.

[60] Singh, A.; Singh, A.; Singh, N.; Jang, D. O. *Tetrahedron* **2016**, *72*, 3535-3541.

[61] Zhou, J.; Yuan, Y.-F.; Zhuo, J.-B.; Lin, C.-X. *Tetrahedron Letters* **2018**, *59*, 1059-1064.

[62] Han, T.; Gu, X.; Lam, J. W. Y.; Leung, A. C. S.; Kwok, R. T. K.; Han, T.; Tong, B.; Shi, J.; Dong, Y.; Tang, B. Z. *Journal of Materials Chemistry C* **2016**, *4*, 10430-10434.

[63] Gandhimathi, S.; Balakrishnan, C.; Theetharappan, M.; Neelakantan, M. A.; Venkataraman, R. *Spectrochimica Acta Part A: Molecular and Biomolecular Spectroscopy* **2017**, *175*, 134-144.

[64] Bhattacharjee, I.; Acharya, N.; Bhatia, H.; Ray, D. *The Journal of Physical Chemistry Letters* **2018**, *9*, 2733-2738.

[65] Wang, Y.; Liu, T.; Bu, L.; Li, J.; Yang, C.; Li, X.; Tao, Y.; Yang, W. *The Journal of Physical Chemistry C* **2012**, *116*, 15576-15583.

[66] Hossain, S. M.; Singh, K.; Lakma, A.; Pradhan, R. N.; Singh, A. K. *Sensors and Actuators B: Chemical* **2017**, *239*, 1109-1117.

[67] Ray, D.; Bharadwaj, P. K. *Inorganic Chemistry* **2008**, *47*, 2252-2254.

[68] Ichiba, H.; Yonei, M.; Sakamoto, T.; Kuwayama, H.; Hamada, Y.; Yamada, H.; Onozato, M.; Hiruta, T.; Nakagawa, H.; Fukushima, T. *Inorganica Chimica Acta* **2015**, *435*, 53-59.

[69] Liu, C.; Liu, L.-m.; Li, T.-r.; Liu, K.; Yang, Z.-y. *Inorganica Chimica Acta* **2020**, *502*, 119327-119332.

[70] Lv, J.; Fu, Y.; Liu, G.; Fan, C.; Pu, S. *RSC Advances* **2019**, *9*, 10395-10404.

[71] Kumar, M.; Kumar, A.; Faizi, M. S. H.; Kumar, S.; Singh, M. K.; Sahu, S. K.; Kishor, S.; John, R. P. *Sensors and Actuators B: Chemical* **2018**, *260*, 888-899.

[72] Xu, Y.; Mao, S.; Peng, H.; Wang, F.; Zhang, H.; Aderinto, S. O.; Wu, H. *Journal of Luminescence* **2017**, *192*, 56-63.

[73] Feng, E.; Lu, R.; Fan, C.; Zheng, C.; Pu, S. *Tetrahedron Letters* **2017**, *58*, 1390-1394.

[74] Xiao, N.; Xie, L.; Zhi, X.; Fang, C.-J. *Inorganic Chemistry Communications* **2018**, *89*, 13-17.

[75] Mabhai, S.; Dolai, M.; Dey, S.; Dhara, A.; Das, B.; Jana, A. *New Journal of Chemistry* **2018**, *42*, 10191-10201.

[76] Kejík, Z.; Kaplánek, R.; Havlík, M.; Bříza, T.; Vavřinová, D.; Dolenský, B.; Martásek, P.; Král, V. *Journal of Luminescence* **2016**, *180*, 269-277.